Article

Cell Systems

Proliferation history and transcription factor levels drive direct conversion to motor neurons

Graphical abstract

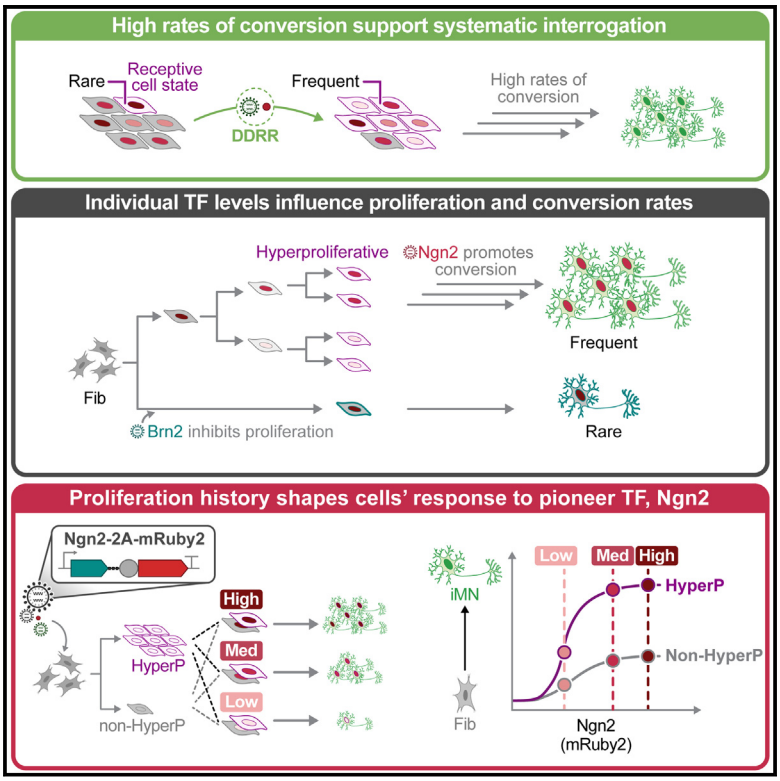

Highlights

- Proliferation history offers a principal axis to distinguish TF effect on fate
- Levels of individual TFs differentially influence the rate of conversion
- Proliferation history shapes the cell's response to levels of pioneer TF, Ngn2
- Driving early hyperproliferation increases direct conversion of adult human fibroblasts

Authors

Nathan B. Wang, Brittany A. Lende-Dorn, Adam M. Beitz, Patrick Han, Honour O. Adewumi, Timothy M. O'Shea, Kate E. Galloway

Correspondence

katiegal@mit.edu

In brief

Using a systems and synthetic biology approach to study the molecular determinants of conversion, Wang et al. find that proliferation history and TF levels drive cell fate in direct conversion to motor neurons.

Wang et al., 2025, Cell Systems *16*, 101205
April 16, 2025
https://doi.org/10.1016/j.cels.2025.101205

CellPress

Cell Systems

CellPress

Article

Proliferation history and transcription factor levels drive direct conversion to motor neurons

Nathan B. Wang,[1] Brittany A. Lende-Dorn,[1] Adam M. Beitz,[1] Patrick Han,[1,3] Honour O. Adewumi,[2] Timothy M. O'Shea,[2] and Kate E. Galloway[1,4,*]

[1]Department of Chemical Engineering, Massachusetts Institute of Technology, Cambridge, MA 02139, USA
[2]Department of Biomedical Engineering, Boston University, Boston, MA 02215, USA
[3]Present address: Integrated Science and Engineering Division, Underwood International College, Yonsei University, South Korea
[4]Lead contact
*Correspondence: katiegal@mit.edu
https://doi.org/10.1016/j.cels.2025.101205

SUMMARY

The sparse and stochastic nature of conversion has obscured our understanding of how transcription factors (TFs) drive cells to new identities. To overcome this limit, we develop a tailored, high-efficiency conversion system that increases the direct conversion of fibroblasts to motor neurons 100-fold. By tailoring the cocktail to a minimal set of transcripts, we reduce extrinsic variation, allowing us to examine how proliferation and TFs synergistically drive conversion. We show that cell state—as set by proliferation history—defines how cells interpret the levels of TFs. Controlling for proliferation history and titrating each TF, we find that conversion correlates with levels of the pioneer TF Ngn2. By isolating cells by both their proliferation history and Ngn2 levels, we demonstrate that levels of Ngn2 expression alone are insufficient to predict conversion rates. Rather, proliferation history and TF levels combine to drive direct conversion. Finally, increasing the proliferation rate of adult human fibroblasts generates morphologically mature induced human motor neurons at high rates.

INTRODUCTION

The inherently stochastic nature of conversion has limited the identification of design rules for guiding cells through cell-fate transitions.[1,2] Combinations of transcription factors (TFs) guide cells to specific new cell fates.[3–16] However, within these diverse cocktails, how the individual TFs and their stoichiometries influence conversion events remains poorly defined.[5,14,15,17–19] Extrinsic variation including variability across batches of cells, complex cocktails of TFs, and copy number, as well as intrinsic cellular variation, have obscured how the levels of individual TFs promote or impede reprogramming.[20,21] Process variability, combined with low rates of reprogramming, constrains our ability to resolve the distinct molecular states and processes that cells adopt during successful reprogramming.[22] By improving the rate of reprogramming, we can identify these states and processes that promote cell-fate transitions.

Across diverse systems, previous work has established that higher expression of reprogramming factors correlates with higher rates of reprogramming.[22–24] However, inclusion or dropout of individual TFs influences the number of reprogramming events, transcriptional trajectories, and function of converted cells.[7,14,25] While transcriptional profiling identifies expression trajectories, TFs exert their influence as proteins, which cannot be directly imputed from mRNA expression.[26–28] Moreover, global processes such as transcription, replication, and proliferation strongly influence reprogramming events and may amplify or dampen the expression and activity of TFs.[20,23,29–33] Thus, TFs are powerful drivers of cellular reprogramming, but how they combine with other global processes to guide cell-fate transitions remains unclear.

During development, progenitor cells often divide prior to differentiation.[34–36] Division supports differentiation and maintenance of the progenitor pool as cells adopt distinct fates. In direct conversion, cells do not necessarily transit through a defined progenitor state,[9,37] and proliferation is not required for conversion.[38–40] However, highly proliferative cells reprogram at higher rates to both induced pluripotent stem cells (iPSCs) and post-mitotic neurons, suggesting that proliferation may serve a conserved role in facilitating cell-fate transitions.[20,23,41] Further, higher rates of proliferation can accelerate reprogramming.[42] Curiously, we and others have observed that the rate of proliferation can substantially impact the expression of TFs in both native and synthetic systems.[23,30] Indeed, in differentiation to macrophages, cell-cycle lengthening enables progenitors to commit to the macrophage lineage by increasing accumulation of PU.1 protein without increasing PU.1 transcription.[30] If higher rates of proliferation simultaneously increase the probability of reprogramming and reduce expression of the TFs, how do cells integrate these incoherent cues?

To examine how individual TFs and their levels of expression contribute to reprogramming outcomes, we selected a model of direct conversion from fibroblasts to motor neurons.[23] Direct conversion to motor neurons provides a well-defined testbed

Please cite this article in press as: Wang et al., Proliferation history and transcription factor levels drive direct conversion to motor neurons, Cell Systems (2025), https://doi.org/10.1016/j.cels.2025.101205

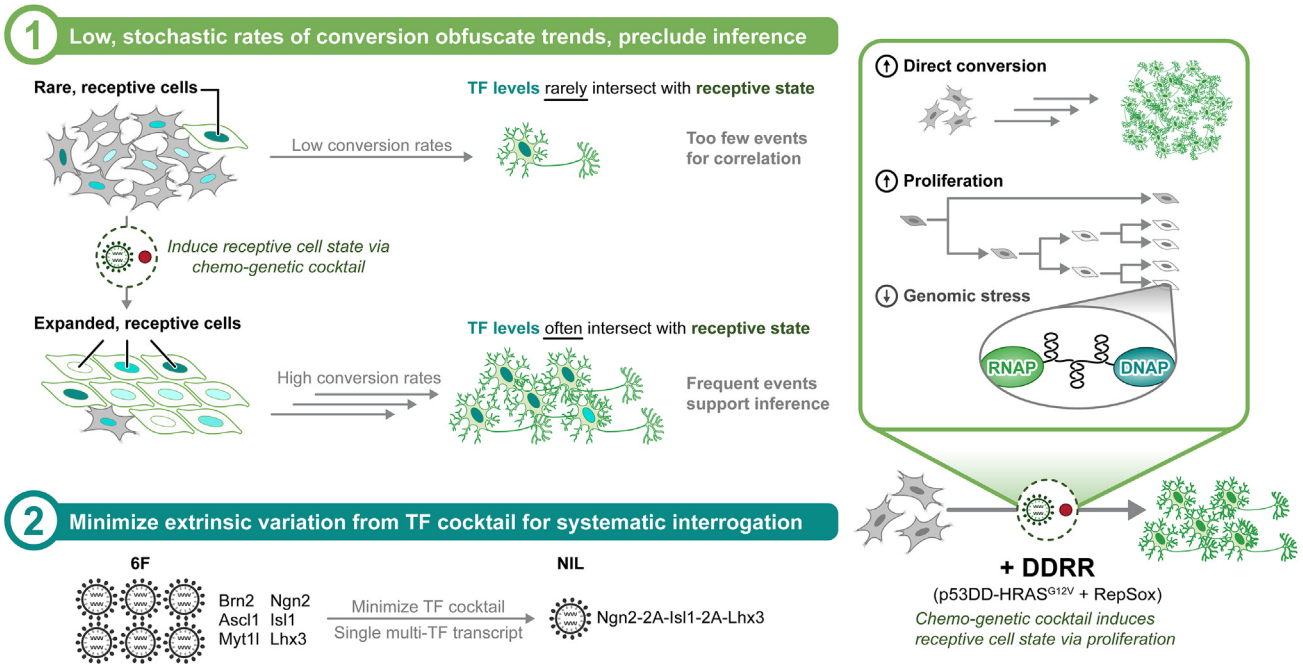

Figure 1. Stochastic and sparse nature of conversion limits understanding

Low, stochastic rates of conversion obfuscate how TFs drive direct conversion. By using a high-efficiency, chemo-genetic cocktail, termed DDRR (p53DD [DD], HRAS^{G12V} [R], and RepSox [R], a small-molecule TGF-β-inhibitor), we are able to induce a cell state that is more receptive to direct conversion, facilitating the study of how TF levels map to conversion outcomes.[23] DDRR induces a more receptive cell state by driving proliferation and reducing genomic stress encountered during conversion. While DDRR significantly increases direct conversion to neural lineages, previous motor neuron direct conversion cocktails contained six different TFs, making it difficult to ascertain their effects on conversion. In this work, we set out to tailor the cocktail to its minimal components to facilitate systematic exploration of how exogenous expression of TFs contribute to cell-fate conversion.

with established mouse transgenic reporters for staging the conversion process in living cells. Importantly, direct conversion to a post-mitotic identity provides several advantages over reprogramming to iPSCs. Conversion to a post-mitotic cell type such as motor neurons allows us to decouple transient changes in proliferation, which facilitate cell-fate transitions, from proliferation rates associated with the new cell identity. Further, we can accurately estimate conversion events based simply on the number of neurons generated, which is not possible in conversion to iPSCs. Unlike iPSCs, neurons do not divide once converted. Thus, each neuron corresponds to exactly one conversion event.

While post-mitotic neurons are useful for quantifying conversion events, direct conversion protocols to non-proliferative cell fates often suffer from low conversion yields. To better dissect how TF levels direct cell-fate transitions, we addressed the challenge of low conversion rates by capitalizing on our recently developed chemo-genetic cocktail that increases direct conversion to motor neurons by two orders of magnitude.[23] Importantly, we first sought to reduce sources of extrinsic variation to resolve how individual TFs influence conversion outcomes. To this end, we tailored the TF cocktail and minimized the number of viruses, consequently increasing the fraction of cells that undergo a period of rapid proliferation. These cells with a hyperproliferative (hyperP) history convert at 4-fold higher rates than non-hyperP cells, leading to an exponential increase in yield. By increasing the number of conversion events and titrating expression, we identified TF-specific correlations between expression and conversion events. Then, by sorting cells on both their proliferation history and their levels of Ngn2, we demonstrated that hyperP cells with similar or even lower levels of the pioneer TF Ngn2 convert at higher rates than non-hyperP cells. Thus, cell state—as set by proliferation history—defines the responsiveness of cells to TF levels. Using these insights, we designed improved conversion cocktails for direct conversion of adult human fibroblasts to motor neurons by increasing proliferation. Overall, we find that proliferation history and TF expression combine to drive cell-fate transitions.

RESULTS

Tailored conversion cocktail minimizes extrinsic variation and increases conversion events

We aimed to minimize sources of extrinsic variation so we could precisely dissect the processes that support cell-fate transitions (Figure 1). Capitalizing on our recently developed high-efficiency cocktail (DDRR: p53DD [DD]; HRAS^{G12V} [R] and the small-molecule transforming growth factor β [TGF-β]-inhibitor RepSox [R]),[23] we used the conversion of mouse embryonic fibroblasts (MEFs) to induced motor neurons (iMNs) as our model system. DDRR is a chemo-genetic cocktail that dramatically improves direct conversion to neural lineages by increasing the fraction of cells that can rapidly proliferate early in conversion while decreasing genomic stress through topoisomerase activation.[23] These cells with a rapid proliferative history are normally rare but more receptive to conversion by TF cocktails. Thus, we

Please cite this article in press as: Wang et al., Proliferation history and transcription factor levels drive direct conversion to motor neurons, Cell Systems (2025), https://doi.org/10.1016/j.cels.2025.101205

CellPress

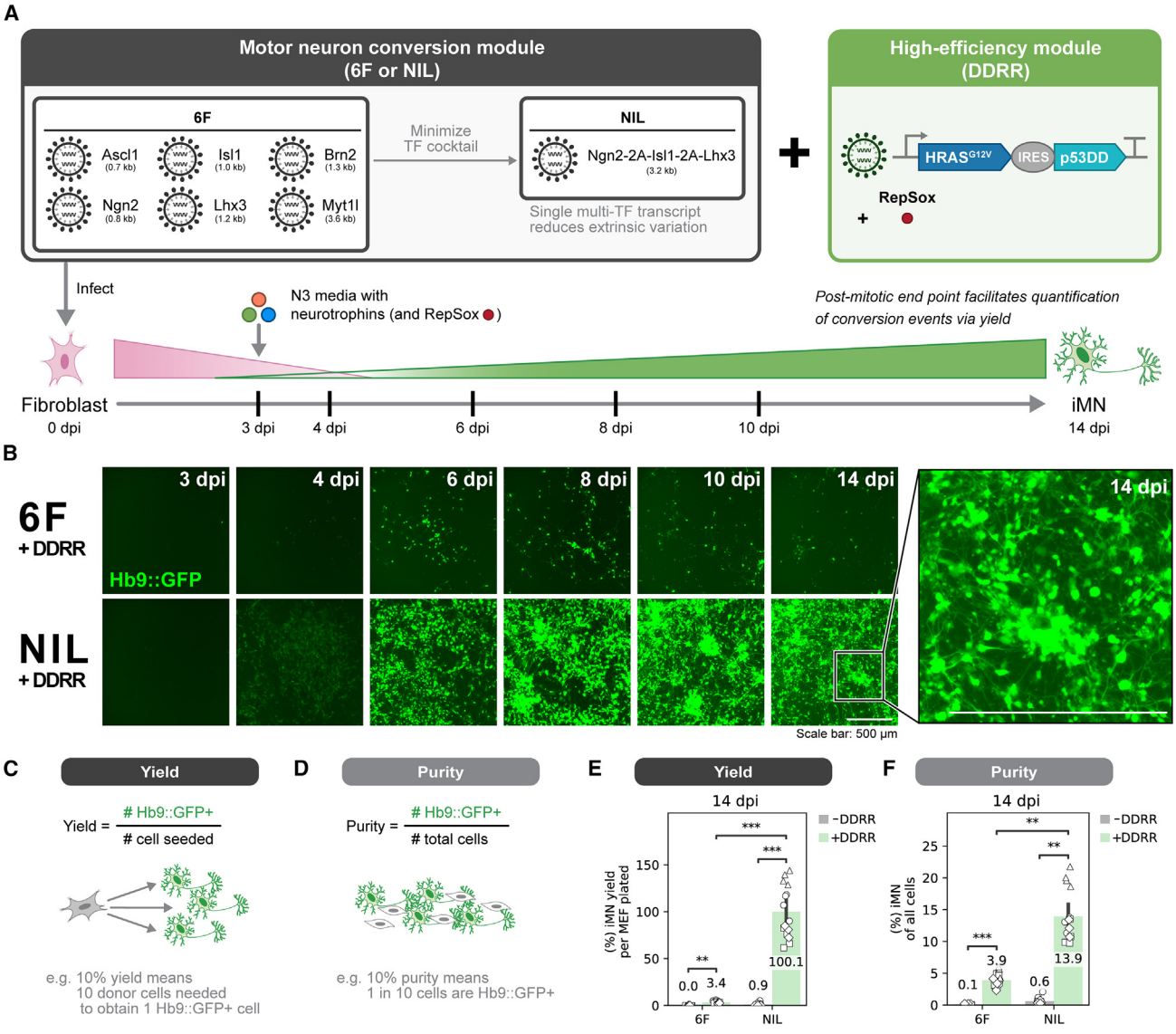

Figure 2. Tailored conversion cocktail minimizes extrinsic variation and increases conversion events

(A) Schematic depicting the conversion process.

(B) Images of Hb9::GFP activation and morphological changes of MEF-to-iMN conversion starting at 3 days post-infection (dpi) until 14 dpi when conversion purity and yield are quantified. Inset shows zoomed-in portion of image. Both scale bars represent 500 μm.

(C and D) Conversion outcomes can be quantified by yield (C) and purity (D). We define yield as the number of bright Hb9::GFP+ cells (Figure S1A) per initial donor cell seeded and purity as the number of bright Hb9::GFP+ cells out of all cells detected.

(E and F) Conversion yield (E) and purity (F) at 14 dpi for 6F vs. NIL ± DDRR. Mean is shown with 95% confidence interval; marker style denotes biological replicates; $n = 4$ biological replicates per condition; one-tailed t test with Bonferroni correction.

Significance summary: $p > 0.05$ (ns); $^{*}p \leq 0.05$; $^{**}p \leq 0.01$; $^{***}p \leq 0.001$; and $^{****}p \leq 0.0001$.

hypothesized that including DDRR to increase the fraction of cells in this receptive state would enable exploration of how individual TFs contribute to cell-fate conversion.

We delivered the conversion factors encoded on retroviruses to transgenic MEFs bearing the motor neuron reporter Hb9::GFP,[43] which allows us to monitor conversion dynamically. Activation of Hb9::GFP and neuronal morphology provide live metrics of the conversion process (Figures 2A, 2B, and S1A). Importantly, each fully converted iMN corresponds to exactly one conversion event, allowing us to quantitatively evaluate how perturbations impact the number of successful events. We delivered the genetic portion of the high-efficiency DDRR module as a single viral cargo to reduce variability caused by differential integration of p53DD and HRAS^{G12V}.[44] To capture multiple dimensions of the conversion process's efficiency, we used two metrics: yield and purity (Figures 2C and 2D). We quantify yield by the number of converted cells at the final time point relative to the starting cell input. Yield increases for highly proliferative conditions and measures how many successful conversion events occur from an initial seeded population. We also quantify

Please cite this article in press as: Wang et al., Proliferation history and transcription factor levels drive direct conversion to motor neurons, Cell Systems (2025), https://doi.org/10.1016/j.cels.2025.101205

purity by the percentage of cells of the total population that is converted at that time point. Purity measures the proportion of the cells at the time of quantification that have converted into the desired cell fate. Yield and purity are generally correlated; however, differences in these metrics may reflect different proliferation rates between cells, such as non-converted and converted iMNs.

While our previously published protocol improved rates of direct conversion, we observed substantial variability across biological replicates.[23] We suspected the variability in conversion rate was due to extrinsic variation introduced by co-transduction of eight different viruses. To reduce extrinsic variation and improve the controllability of the cocktail, we minimized the number of TFs and viruses. First, we sought to identify the minimal set of TFs from the originally identified six factors (6F: Brn2, Ascl1, Myt1l, Ngn2, Isl1, and Lhx3) that could induce iMN fate with our previously identified high-efficiency cocktail.[9,23] Induction of Ngn2, Isl1, and Lhx3 (NIL) expression efficiently drives mouse embryonic stem cells to motor neurons.[45] Further, NIL can be expressed from a single-transcript cassette where each TF is separated by "self-cleaving" 2A sequences.[45] As a 3.2-kb cargo, these three TFs can be efficiently delivered by a single retrovirus to induce conversion (Figure 2A). We verified that NIL together comprise a minimally sufficient set for high-efficiency MEF-to-iMN direct conversion through a TF dropout experiment (Figures S1B and S1C). Interestingly, NIL accelerated the number of Hb9::GFP-positive cells that formed beginning at 4 days post-infection (4 dpi), compared with 6F, with the high-efficiency DDRR cocktail (Figure 2B). Compared with 6F, NIL increases the conversion yield ~30-fold and purity ~4-fold (Figures 2E and 2F).

Having identified a highly efficient and minimal set of TFs for iMN conversion, we set out to systematically examine how individual TFs impact conversion. By reducing extrinsic sources of variability, we developed a highly robust process for the direct conversion of fibroblasts to post-mitotic motor neurons, providing us with a tool to systematically interrogate how TF levels correlate to conversion events.

Proliferation history provides a principal axis to distinguish TFs' influence on conversion

Rapidly proliferating cells convert at higher rates to both mitotic and post-mitotic identities, establishing hyperproliferation as a powerful driver of diverse cell-fate transitions.[20,23,41] Potentially, different conversion rates induced by different TF cocktails can be attributed to cells integrating a differential set of molecular interactions that leads to different rates of proliferation.

To examine whether differences in proliferation rates might distinguish cocktails' conversion rates, we measured the proliferation history of cells undergoing conversion in the presence of 6F or NIL, with and without DDRR. Cells that undergo a period of hyperproliferation were identified by assaying dilution of CellTrace dye for 72 h from 1 to 4 dpi, an early time point in iMN direct conversion as previously established[23] (Figure 3A). We denote cells with a history of rapid proliferation at 4 dpi as hyperP and all other cells at 4 dpi as non-hyperP. We quantify hyperproliferation by both the percentage of cells in the population that are hyperP and the total number of hyperP cells. As expected, the fraction and total number of hyperP cells scale exponentially (Figure 3B). In addition, as we expect from its higher conversion rate (Figures 2E and 2F), NIL + DDRR has a higher fraction and number of hyperP cells than 6F + DDRR (Figures S2A and S2B).

To examine conversion rates for cells with different proliferation histories, we isolated and replated the hyperP and non-hyperP cells at 4 dpi and measured conversion at 14 dpi (Figures 3A, S2C, and S2D). Compared with non-hyperP cells, hyperP cells converted with NIL + DDRR were 10-fold more likely to express Hb9::GFP early on at 4 dpi (Figure 3C) and achieved higher conversion yield and purity (Figures 3D and S2E). By normalizing yield to the number of cells replated at 4 dpi rather than the number of cells initially seeded, we can quantify the probability of cells converting based on proliferation history. A history of early hyperproliferation increases the probability of cells successfully converting by 4-fold in NIL + DDRR (Figure 3D). Further, compared with non-hyperP cells, hyperP cells adopt a more mature, neuronal morphology at 14 dpi, displaying compact, regular soma with interconnected networks of axons (Figures 3E–3G and S2D). Interestingly, early Hb9::GFP activation is not detectable with conversion cocktails other than NIL + DDRR (Figure 3C). Correspondingly, yields after replating at 14 dpi are also low, although hyperP cells converted with 6F + DDRR also convert at higher rates relative to the non-hyperP population (Figures 3D and S2E). Taken together, these data show that not only does hyperproliferation generate more cells but also that the cells generated during hyperproliferation possess a greater ability to convert and develop mature morphologies.

We wondered whether increased rates of hyperproliferation in NIL compared with 6F coincide with a more rapid adoption of the iMN cell fate. To assess the dynamics of conversion events, we tracked Hb9::GFP expression over the conversion process. When DDRR is included with either the NIL or 6F cocktails, Hb9::GFP activation begins at 4 dpi (Figure 2B). For 6F + DDRR, both the number and fraction of Hb9::GFP-positive cells plateau around 5 dpi (Figure 3H). Thus, most conversion events occur early with 6F + DDRR. In contrast, cells converted with NIL + DDRR continue to generate Hb9::GFP-positive cells throughout the conversion process. We confirmed that adding DDRR to the base NIL cocktail induces a transient window of hyperproliferation by immunofluorescent staining of Ki67, a marker of proliferation (Figures S2F–S2K). By 14 dpi, with or without DDRR, the majority of Hb9::GFP-positive cells do not express Ki67 (Figures S2I–S2K). Expanding the conversion window not only increases the yield of converted cells but also increases the fraction of cells that are converted (Figure 3H).

To confirm that Hb9::GFP-positive cells commit to a post-mitotic neural identity, we sorted NIL + DDRR Hb9::GFP-positive cells at 14 dpi and replated them with 7 days recovery. We then fed the cells with 5-ethynyl-2′-deoxyuridine (EdU) to quantify DNA synthesis indicative of cell-cycle progression, performing a 24-h treatment for increased sensitivity. We also used the DNA synthesis inhibitor, aphidicolin, as a control to account for baseline EdU uptake during the long EdU treatment period. We used a proliferative-DDRR-only condition as a positive control and an aphidicolin-treated NIL + DDRR, Hb9::GFP-positive-sorted condition as a negative control. At 1 week post Hb9::GFP-sort, we observed a small fraction (<5%) of residually

Please cite this article in press as: Wang et al., Proliferation history and transcription factor levels drive direct conversion to motor neurons, Cell Systems (2025), https://doi.org/10.1016/j.cels.2025.101205

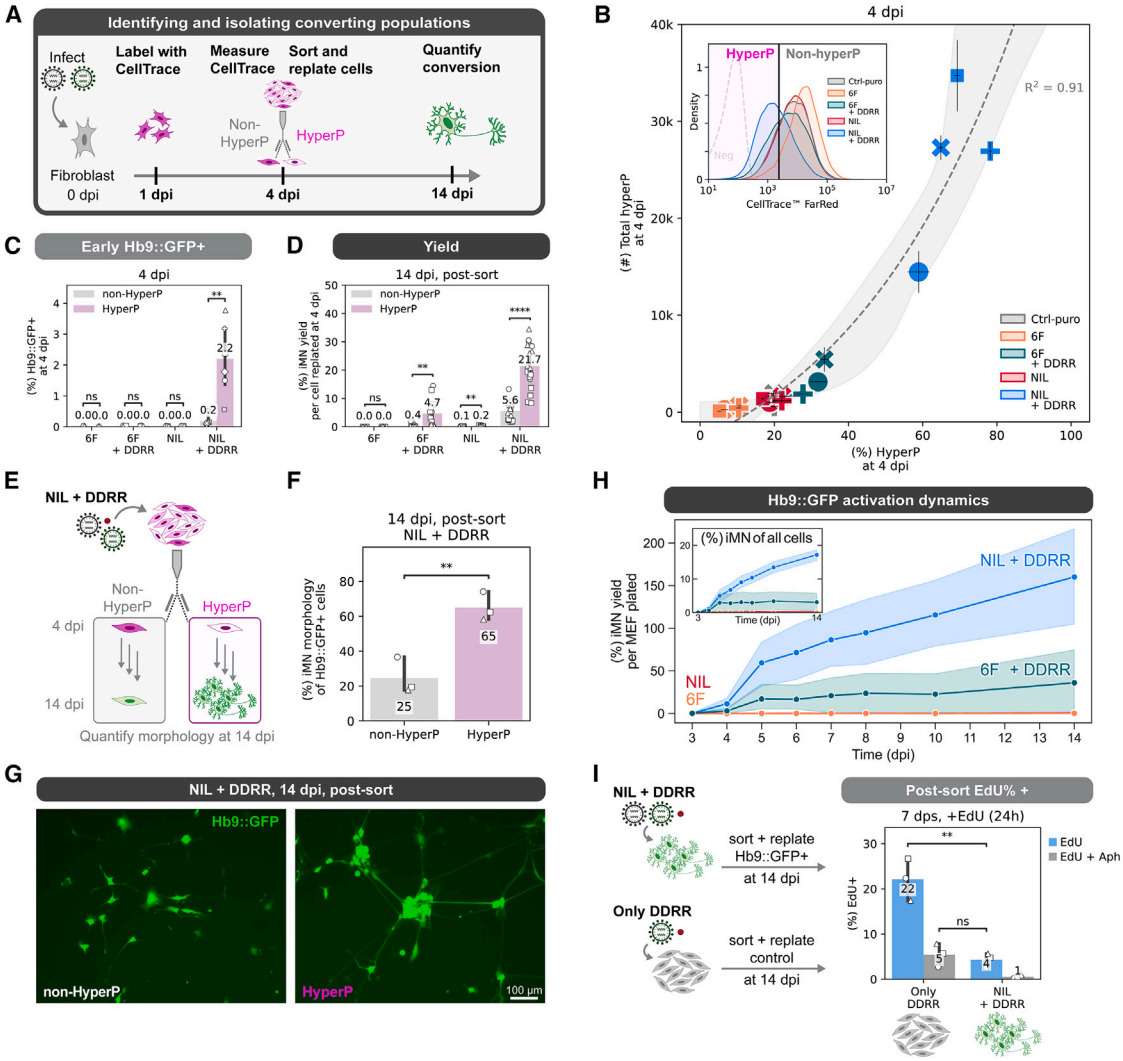

Figure 3. Proliferation history provides a principal axis to distinguish TFs' influence on conversion

(A) Schematic of the CellTrace dilution assay. Cells are labeled at 1 dpi, and their fluorescent intensity is measured at 4 dpi. Cells that have gone through many divisions have low fluorescence. For sorting experiments, cells are sorted at 4 dpi into hyperP and non-hyperP according to their fluorescent intensity relative to a control puro-infected condition for a given biological replicate. Cells are replated on 4 dpi at the same initial seeding density at 10,000 cells/96-well.

(B) HyperP total number vs. percentage at 4 dpi across all conversion conditions. An exponential fit is shown with 95% confidence interval. Representative CellTrace distributions across conversion conditions. HyperP cells are defined relative to the 20%-lowest fluorescent cells in a control puro (Ctrl-puro)-infected condition for a given biological replicate; marker style denotes biological replicates; $n = 4$ biological replicates per condition.

(C) Early Hb9::GFP reporter expression at 4 dpi in hyperP vs. non-hyperP populations within each condition. Mean is shown with 95% confidence interval; marker style denotes biological replicates; $n = 3$–6 biological replicates per condition; one-tailed t test.

(D) Conversion yield at 14 dpi for cells sorted and replated at the same initial seeding density at 10,000 cells/96-well into hyperP vs. non-hyperP populations within each condition. Mean is shown with 95% confidence interval; marker style denotes biological replicates; $n = 3$ biological replicates per condition; one-tailed t test.

(E–G) (E) Cells converted with NIL + DDRR were sorted from hyperP and non-hyperP at 4 dpi to compare the morphologies of the resulting Hb9::GFP+ cells at 14 dpi. (F) Percentage of Hb9::GFP+ cells with a neuronal morphology (tight soma with neurites) were quantified from randomly sampled images. >100 Hb9::GFP+ cells were quantified for each of $n = 3$ biological replicates per condition; one-tailed t test. (G) Representative images, scale bar represents 100 µm.

(H) Yield of cells activating Hb9::GFP reporter expression from 3 to 14 dpi for 6F vs. NIL ± DDRR. Inset shows the purity over time. Mean is shown with 95% confidence interval. $n = 3$ biological replicates per condition.

(I) Hb9::GFP-positive cells converted with NIL + DDRR were sorted and replated at 14 dpi to test for residual proliferative capacity. After 7 days post-sort (dps) for recovery, EdU was fed for 24 h. Treatment with aphidicolin (aph) to block DNA synthesis was used as a negative control. DDRR-only induced cells were replated also as a positive control for proliferation. Mean is shown with 95% confidence interval; marker style denotes biological replicates; $n = 3$ biological replicates per condition.

Significance summary: $p > 0.05$ (ns); $^{*}p \leq 0.05$; $^{**}p \leq 0.01$; $^{***}p \leq 0.001$; and $^{****}p \leq 0.0001$.

Please cite this article in press as: Wang et al., Proliferation history and transcription factor levels drive direct conversion to motor neurons, Cell Systems (2025), https://doi.org/10.1016/j.cels.2025.101205

proliferative cells (Figure 3I). This is less than the percentage of proliferative DDRR cells (~22%) and similar to the percentage of aphidicolin-stalled DDRR cells (~5%), indicating that a small fraction of cells that activate the Hb9::GFP reporter may still divide, but the majority adopt a post-mitotic identity.

Altogether, our data suggest a model in which driving proliferation provides an exponential benefit in the conversion to iMNs. Proliferation not only expands the number of cells but also endows this expanded population with a greater propensity to convert. Despite the transduction with powerful oncogenes that induce proliferation, TFs drive the majority of converted Hb9::GFP-positive cells to a post-mitotic identity within weeks.

TF identity and encoding impact proliferation and affect conversion rates and dynamics

As TFs can work synergistically, we wondered if differences in conversion rates between the 6F and NIL cocktails were due to a single or to multiple TFs. Given that the 6F cocktail generates less hyperP cells than NIL, with or without DDRR (Figures S2A and S2B), we hypothesized that one or multiple of the three Brn2, Asl1, Myt1L (BAM) TFs may impede proliferation (Figure 4A). Using NIL with the high-efficiency DDRR cocktail as the reference, we added all six possible combinations of the three BAM factors to assess their individual and combined effects on proliferation and conversion. Inclusion of Brn2 reduces proliferation, activation of Hb9::GFP at 4 dpi, and conversion yield and purity (Figures 4B–4D and S3A–S3C). In contrast, the addition of Ascl1 increases iMN yield without altering proliferation (Figures 4D and 4E). Myt1l sometimes increases iMN yield with varying effects on proliferation. These data suggest that individual TFs can independently or synergistically influence proliferation and conversion.

Given that Brn2 strongly limits proliferation even with the addition of the DDRR module, we wondered whether differences in Brn2 expression could contribute to conversion variability. To more closely examine how Brn2 affects conversion, we used a fluorescent Brn2-2A-mRuby2 reporter to track Brn2 expression in NIL + DDRR conversion (Figure 4F). A fluorescent mRuby2 reporter without Brn2 was used as a negative control. To assess how variable Brn2 expression can lead to different conversion rates by reducing proliferation, we added Brn2-2A-mRuby2 at a low multiplicity of infection (MOI = 0.1) and at a high MOI (MOI = 5) to obtain heterogeneous and homogeneous Brn2 conversion populations, respectively (Figure 4G). As expected, the high-MOI Brn2 condition had fewer hyperP cells and lower yield than the low-MOI Brn2 and control mRuby2 conditions (Figure 4H).

To verify that differences in Brn2 expression led to the observed differences in proliferation and conversion yield, we isolated mRuby2-positive cells in our analysis and compared them with the bulk population. At 4 dpi, the total cell count of bulk and mRuby2-positive cells are indistinguishable for the homogeneous, high-MOI Brn2 and mRuby2-only control conditions (Figure 4J), indicating that nearly all cells expressed these transgenes as expected. Correspondingly, proliferation rates are consistent in the bulk population as compared with just the mRuby2-positive cells at 4 dpi for the high-MOI Brn2 condition and the mRuby2-only control (Figures S3D–S3H). In contrast, the heterogeneous, low-MOI Brn2 condition shows a decrease in the fraction of hyperP cells in the Brn2-2A-mRuby2-positive cells as compared with the bulk. In addition, high-MOI Brn2 has higher Brn2-2A-mRuby2 expression than low-MOI Brn2 conditions (Figures S3I and S3J) Thus, Brn2 limits proliferation in a manner dependent on its expression level.

For a given biological replicate, we assayed twin plates at 4 and 14 dpi for proliferation and conversion rates, respectively, as well as for Brn2-2A-mRuby2 expression. By normalizing conversion yield of Brn2-2A-mRuby2-positive cells at 14 dpi to the number of Brn2-2A-mRuby2-positive cells at 4 dpi, we can account for differences in the number of infected cells across MOIs (Figures 4I and 4J). We observed that Brn2 reduces the number of converted cells at 14 dpi obtained from a NIL + DDRR-converting background at 4 dpi (Figure 4K). Together, these data show that Brn2 expression reduces proliferation and conversion in a manner dependent on its level of expression. Putatively, variation in Brn2 expression across cells and replicates may explain the lower and variable conversion rates from the 6F motor neuron conversion cocktail.

In addition, we found that the encoding of the TF cocktail, not just the identity of the constituents, impacts conversion. The cocktails of 6F and NIL + BAM contain an identical set of TFs. However, in 6F, Ngn2, Isl1, and Lhx3 are expressed from separate transcripts, whereas NIL expresses the same factors from a single transcript. With DDRR, the NIL + BAM cocktail converts with 12-fold higher yield and 7-fold higher purity than the 6F cocktail (Figures 4D and S3C). These data suggest that TF encoding can substantially improve (or hinder) a cocktail's efficacy. Putatively, a single transcript design may improve conversion rates by controlling for co-delivery and stoichiometry and/or by reducing the number of viruses.[44] Together, these observations demonstrate that while the identity of the TFs strongly influences conversion, the encoding and delivery of those factors also impact conversion rates. With that in mind, we sought to determine how each of the three motor neuron TFs (NIL) influences the number of iMNs.

Titration of individual TFs reveals factor-specific influence on conversion rates

To investigate how the levels of exogenous TF expression influence conversion, we titrated individual TFs, while keeping the other genetic cargos constant (Figures 5A and 5B). We used arrays of small upstream open reading frames (uORFs) to generate a range of individual TF levels from otherwise identical retroviral delivery vehicles. uORFs change gene expression by altering translation rates.[46,47] By adding a fluorescent 2A-mRuby2 downstream of the TF (Figure 5B), we built single-cell, live reporters of exogenous TF levels. The mRuby2 levels provide a proxy for the exogenous expression of the linked TF early in the conversion process at 4 dpi. Using these tools, we titrated the level of each TF while keeping other factors and the high-efficiency DDRR module constant. We also used an HA-tagged Ngn2 variant ($Ngn2^{x3HA}$) that we found was more potent in direct conversion than untagged Ngn2.[44]

Consistent with our previous observations,[23,44] the expression of each of the three TF-2A-mRuby2 transgenes are lower in cells that undergo a period of hyperproliferation, compared with cells that do not (Figure 5C). Because we find hyperP cells are 10-fold more likely to activate Hb9::GFP early and 4-fold more likely to convert to morphologically mature, motor neurons

Please cite this article in press as: Wang et al., Proliferation history and transcription factor levels drive direct conversion to motor neurons, Cell Systems (2025), https://doi.org/10.1016/j.cels.2025.101205

CellPress

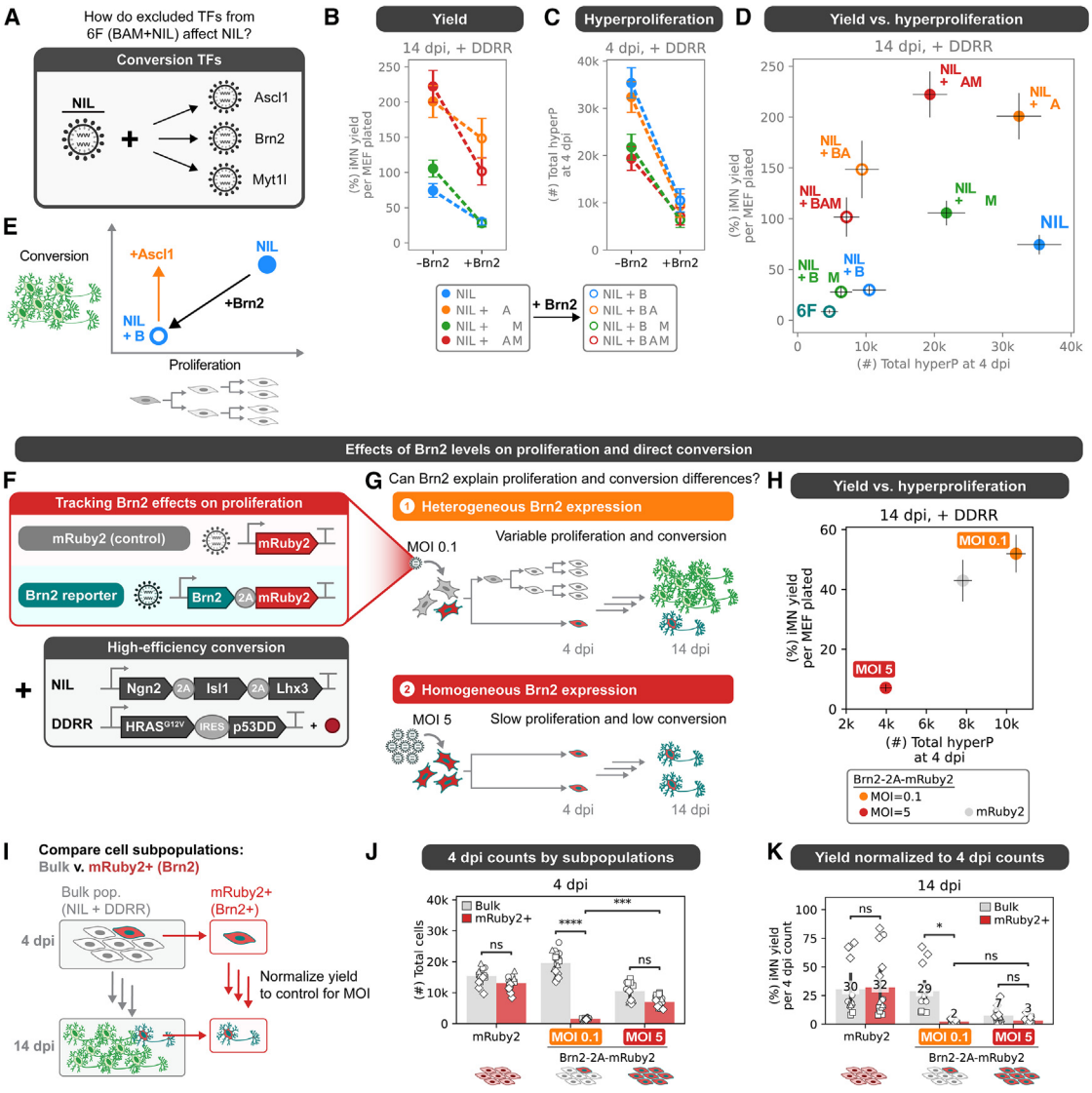

Figure 4. TF identity and encoding impact proliferation and affect conversion rates and dynamics

(A–D) Each TF from the 6F cocktail was added onto NIL + DDRR to identify which TF(s) reduces conversion in 6F vs. NIL + DDRR. Brn2's effect on (B) conversion yield and (C) hyperproliferation at 4 dpi for each conversion cocktail and encoding (all converted with DDRR). Dashed lines connect cocktails without Brn2 (closed circle) to corresponding ones with Brn2 (open circle). (D) Conversion yield at 14 dpi vs. total number of hyperP cells at 4 dpi for each conversion cocktail (all converted with +DDRR). Mean is shown ± standard error of mean (SEM); $n = 4$ biological replicates per condition.

(E) Diagram of model that Brn2 reduces proliferation and conversion, while addition of Ascl1 improves conversion yield by non-proliferation-mediated mechanisms.

(F–H) (F) Variable Brn2 expression during conversion was explored using a Brn2-2A-mRuby2 fluorescent reporter with NIL + DDRR as the base conversion cocktail. A control mRuby2 fluorescent reporter lacking Brn2 was also used to account for burden on cells. (G) Cells were transduced with either a low MOI (MOI = 0.1) or high MOI (MOI = 5) to simulate heterogeneous or homogeneous expression during conversion, respectively. (H) Conversion yield at 14 dpi vs. total number of hyperP cells at 4 dpi. Mean is shown ± SEM; $n = 4$ biological replicates per condition.

(I–K) (I) Overview of coupled time point (4 and 14 dpi) approach for measuring Brn2 effects on proliferation and conversion. Cells are converted in biological duplicates where one twin is assayed at 4 dpi to measure proliferation and expression of the mRuby2 reporter (Figures S3D–S3J). The other twin is kept until 14 dpi to measure conversion rates. This twin assay approach is used to calculate a normalized yield (K) as the 14 dpi yields in (H) normalized to the 4 dpi counts in (J) of the entire bulk sample or just the mRuby2+ cells in each condition and biological replicate. This normalization accounts for the lower number of cells transduced with the mRuby2 reporter in the low-MOI (orange) condition, compared with the high-MOI (red) and control mRuby2 (gray) conditions. Mean is shown with 95% confidence interval; marker style denotes biological replicates; $n = 4$ biological replicates per condition; two-tailed t test.

Significance summary: $p > 0.05$ (ns); $^{*}p \leq 0.05$; $^{**}p \leq 0.01$; $^{***}p \leq 0.001$; and $^{****}p \leq 0.0001$.

(Figures 3C–3G), we chose to examine the transgene expression within this population of hyperP cells. Isolating the hyperP cells allowed us to eliminate the confounder of different levels of expression across subpopulations of cells. Thus, we expect that trends observed in these more receptive cells will most clearly reveal the influence of TF levels on conversion events.

Please cite this article in press as: Wang et al., Proliferation history and transcription factor levels drive direct conversion to motor neurons, Cell Systems (2025), https://doi.org/10.1016/j.cels.2025.101205

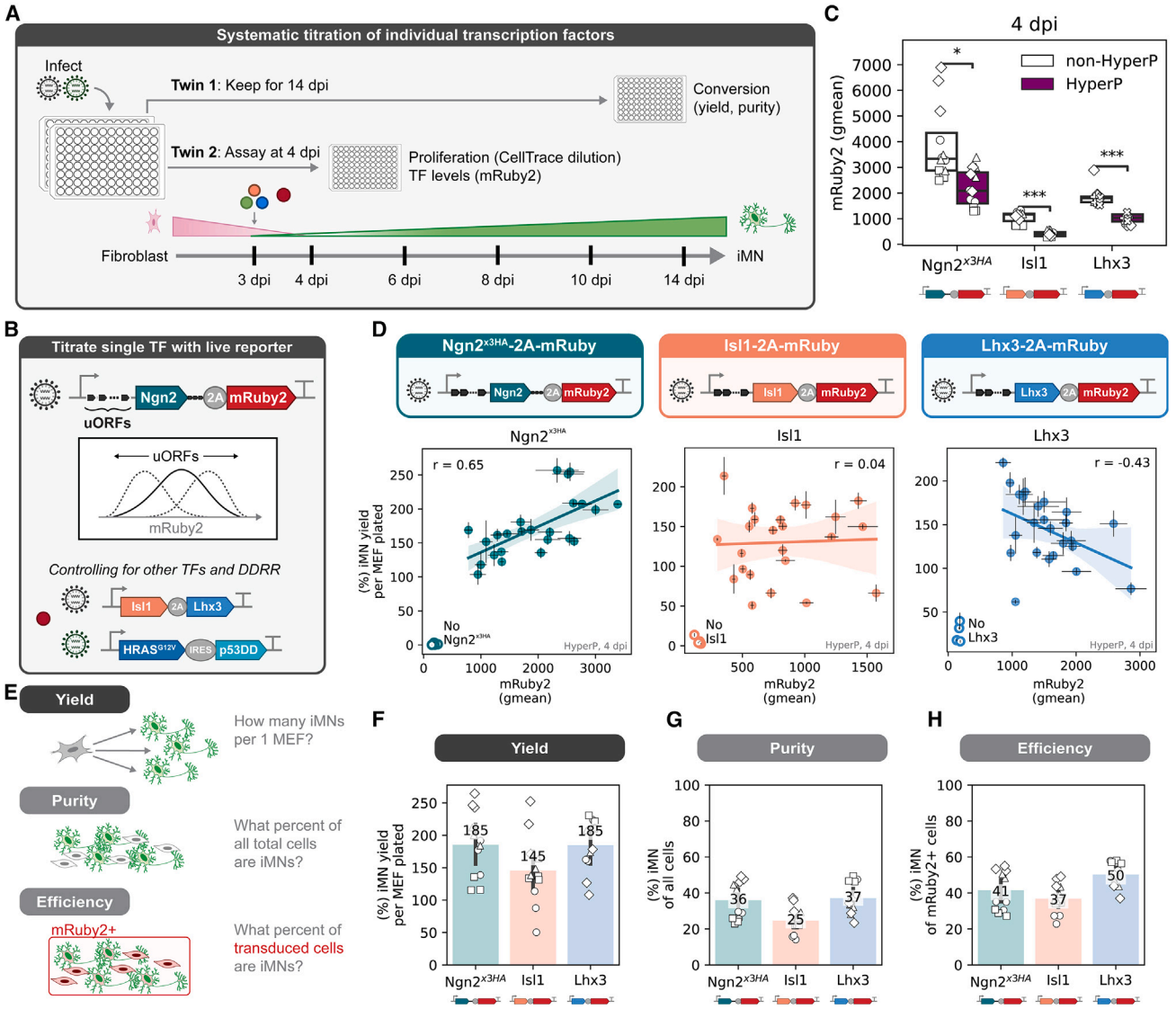

Figure 5. Titration of individual TFs reveals factor-specific influence on conversion rates

(A) Overview of coupled time point (4 and 14 dpi) approach for titrating TF expression. Cells are converted into biological duplicates where one twin is assayed at 4 dpi to measure expression of the mRuby2 reporter in hyperproliferative cells. The other twin is kept until 14 dpi to measure conversion rates.

(B) Schematic of how individual TF levels were titrated and measured using upstream open reading frames (uORFs) placed upstream of the conversion TF of interest with a 2A-mRuby2 fluorescent reporter. All other factors were kept constant, e.g., if Ngn2^{x3HA}-2A-mRuby2 is titrated, then Isl1, Lhx3, and +DDRR expression are not altered using uORFs.

(C) Expression of TF of interest with a 2A-mRuby2 fluorescent reporter in non-hyperproliferative (non-HyperP) and hyperproliferative (HyperP) cells at 4 dpi. Cells are converted with non-fluorescent versions of the other TFs (e.g., Ngn^{x3HA}-2A-mRuby2 is converted with Isl1, Lhx3, and +DDRR; see B). Geometric mean is shown by markers with a boxplot; markers denote biological replicates; $n = 4$ biological replicates per condition; one-tailed t test.

(D) iMN yield at 14 dpi vs. mRuby2 expression in just the hyperP cells at 4 dpi to avoid confounding proliferation with expression across all uORFs for Ngn^{x3HA}-2A-mRuby2 (left), Isl1-2A-mRuby2 (middle), and Lhx3-2A-mRuby2 (right). Open marker denotes the conditions where the TF-2A-mRuby2, being titrated, is excluded, but all other factors are included. Linear regression with 95% confidence interval; mean is shown ± SEM for each uORF for a single biological replicate; $n = 4$ biological replicates per condition.

(E–G) (E) iMN yield, (F) purity, and (G) efficiency at 14 dpi for each TF-2A-mRuby2 fluorescent reporter with no uORFs. Cells are converted with non-fluorescent versions of the other TFs (e.g., Ngn^{x3HA}-2A-mRuby2 is converted with Isl1, Lhx3, and +DDRR; see B). Efficiency is calculated similar to purity (see Figure 2D), but only transduced cells (i.e., mRuby2+) are considered. Mean is shown ± 95% confidence interval; markers denote biological replicates; $n = 4$ biological replicates per condition.

Significance summary: $p > 0.05$ (ns); $^{*}p \leq 0.05$; $^{**}p \leq 0.01$; and $^{***}p \leq 0.001$.

Please cite this article in press as: Wang et al., Proliferation history and transcription factor levels drive direct conversion to motor neurons, Cell Systems (2025), https://doi.org/10.1016/j.cels.2025.101205

To obtain a range of expression levels, we introduced five different uORFs upstream of the coding sequence of each TF encoded with a mRuby2 reporter (Figure 5B). To exploit natural biological heterogeneity in expression and control for variance across conversion biological replicates, we paired two assays to generate biological twins to more precisely match early expression level with the later conversion outcome. In the first twin, we measured expression and proliferation profiles at 4 dpi, and in the second biological twin, we measured conversion outcomes at 14 dpi (Figure 5A). Importantly, systematically changing TF expression in our tailored conversion module does not affect proliferation rates (Figure S4A). Thus, our designs remove differences in proliferation history as a confounding variable across the genetic variants. As expected, introducing uORFs to transgenes preserves the trend of lower expression in the hyperP cells (Figure S4B).

Using our twin conversion assays, we found that high levels of exogenous Ngn2^{x3HA} lead to improved conversion yields, while exogenous Isl1 expression is uncorrelated with yield (Figure 5D). Comparing across all three TF reporters as controls for one another, conversion rates do not simply correlate with high expression of the mRuby2 reporter, suggesting the TF factor identity sets the relationship between expression and conversion. The positive correlation of conversion yield with expression of the pioneer factor, Ngn2^{x3HA}, mirrors observations from iPSC conversion where high expression of the pioneer factor, Oct4, increases the rate of colony formation.[14] As expected, Ngn2^{x3HA}-2A-mRuby2 expression varies across biological replicates, yet within each biological replicate, the correlation between yield and levels of Ngn2 is preserved (Figure S4C). Surprisingly, we found that exogenous Lhx3 induces a biphasic response in conversion yield (Figure 5D). In the absence of exogenous Lhx3, conversion rates are low. However, high expression of exogenous Lhx3 decreases conversion yield. Putatively, moderate levels of Lhx3 expression support optimal conversion. Together, our data suggest that in the presence of Isl1, a combination of high levels of Ngn2 and low levels of Lhx3 promotes conversion to iMNs. Notably, the trends we observed in the hyperP population were diminished when examining the non-hyperP cells, highlighting the utility of isolating populations with inherently different conversion propensities (Figure S4D). Correlations are also diminished between 14 dpi mRuby2 and 14 dpi conversion rates (Figure S4E). Thus, we find that profiles of TFs are most predictive within specific subpopulations and time windows, highlighting a challenge in parsing dynamic changes in heterogeneous cultures.

For situations where transgene delivery is poor, such as *in vivo* conversion, it is useful to know conversion rates normalized to the number of transduced cells to account for the efficiency of transgene delivery. Using the fluorescent mRuby2 reporter to identify cells expressing the transgenes, we measured the conversion efficiency for each TF reporter. We quantify efficiency as the percentage of converted cells normalized to the number of cells expressing the delivered genetic cargo at 14 dpi (i.e., mRuby2-positive) (Figure 5E). We achieve high efficiency, as 37%–50% of all transgene-expressing cells at 14 dpi convert to iMNs. As expected, conversion purity and efficiency are similar for a given TF encoding (Figures 5F–5H). Given that *in vitro* retroviral delivery to MEFs is highly efficient, the majority of cells are transduced. Thus, it is not surprising that accounting for transduction efficiency in calculating conversion efficiency produces similar rates as conversion purity.

Proliferation history alters the transfer function between TF levels and direct conversion rates

Cell-state determinants such as proliferation history influence cell responses.[20,23,41] Yet, how much can cell state transform the ability of TFs to drive new fates?[30] TFs are essential to drive cell-fate conversion. We found a positive correlation between expression levels of the pioneer factor Ngn2 and conversion, so we expect that higher levels of expression will translate to higher yields. However, hyperP cells express the exogenous TFs at lower levels (Figure 5C) but are more likely to convert to morphologically mature, motor neurons (Figures 3D–3G). To investigate how cells interpret these seemingly incoherent cues, we sorted cells based on their proliferation history and expression levels of pioneer TF, Ngn2. Rather than using uORFs to change expression, we delivered a single Ngn2^{x3HA}-2A-mRuby2 construct with Isl1-2A-Lhx3 and DDRR, then sorted cells at 4 dpi by mRuby2 expression level and proliferation history (Figures 6A and 6B). We replated these sorted subpopulations at 10,000 per 96-well and measured conversion at 14 dpi. Populations with high, medium, and low levels of Ngn2 were defined as the brightest 75%–100%, medium 50%–75%, and dimmest 0%–25% mRuby2-expressing cells, respectively, and were then further split by proliferation history. By definition, each Ngn2 category sums to 25% across both hyperP and non-hyperP subpopulations (Figure 6C). As expected, the hyperP cells are enriched with Ngn2^{x3HA}-2A-mRuby2-low cells, while non-hyperP cells are enriched with Ngn2-high-expressing cells (Figure 5C). In addition, cells maintain their relative mRuby2 expression levels through 14 dpi, suggesting that relative Ngn2^{x3HA}-2A-mRuby2 levels are consistent with sorted subpopulations from 4 to 14 dpi (Figure S5A).

By measuring the conversion rates of 4 dpi replated subpopulations at 14 dpi, we were able to approximate a transfer function of Ngn2 level and proliferation history at 4 dpi to conversion rate at 14 dpi (Figure 6D). We found that hyperP cells convert at higher rates than non-hyperP cells. Cells from higher Ngn2-expressing subpopulations generally convert at higher rates within each proliferative category (Figures 6D, 6E, and S5B). However, even with lower levels of Ngn2, hyperP cells with medium levels of Ngn2 convert at higher rates than non-hyperP cells with high levels of Ngn2. Similarly, hyperP cells that are Ngn2-low convert at similar rates to non-hyperP cells with high levels of Ngn2. Thus, the conversion potential of cells with the same levels of Ngn2 can be distinguished and defined by their proliferation histories.

Driving hyperproliferation improves direct conversion of adult human fibroblasts

Having identified a compact cocktail that reduces variability and increases the yield of motor neurons from mouse cells, we wondered how these cocktails might impact conversion of primary adult human dermal fibroblasts (HDFs), where yields and maturities remain limited.[23] As direct conversion of primary human fibroblasts offers a powerful platform for disease modeling and drug discovery, improved rates of conversion are essential for using these converted surrogate cells for

Please cite this article in press as: Wang et al., Proliferation history and transcription factor levels drive direct conversion to motor neurons, Cell Systems (2025), https://doi.org/10.1016/j.cels.2025.101205

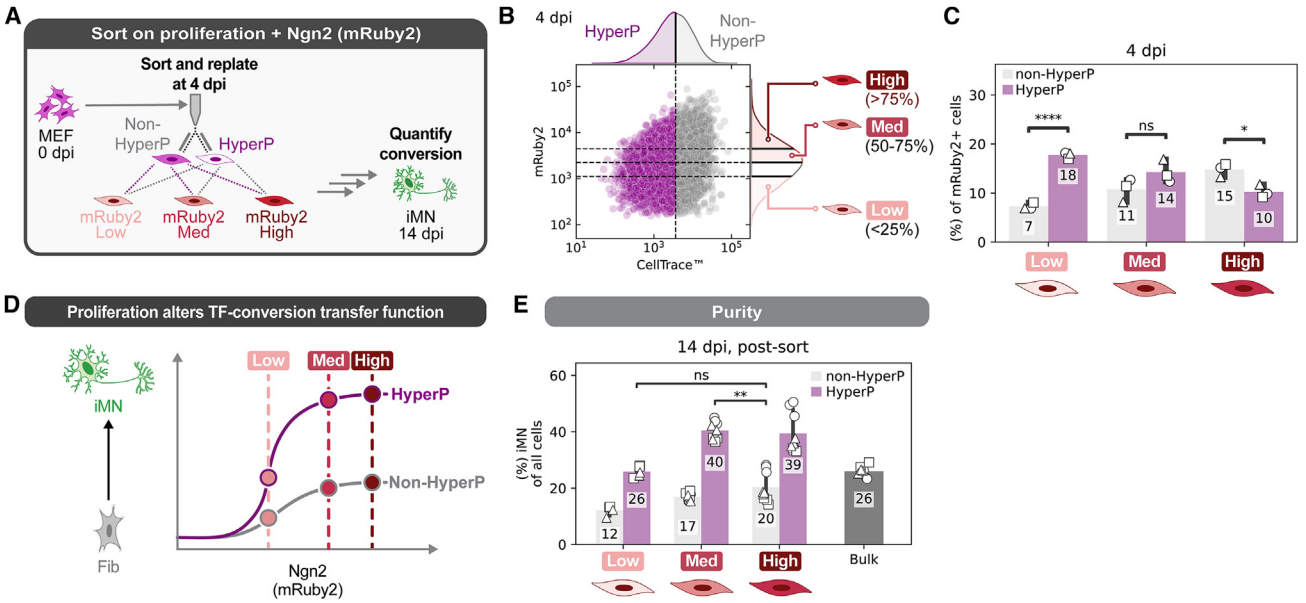

Figure 6. Proliferation history alters transfer function between TF levels and direct conversion rates

(A) Overview of sorting strategy to predict conversion outcomes based on proliferation history and TF expression at 4 dpi and converted until 14 dpi. Like in Figure 5D, cells were converted with Ngn2^{x3HA}-2A-mRuby2, Isl1-2A-Lhx3, and +DDRR. Cells were sorted at 4 dpi by their mRuby2 (Ngn2^{x3HA}) expression and their proliferation history.

(B and C) A representative flow plot of hyperP and Ngn2 (mRuby2) sorted by fluorescence-activated cell sorting (FACS). High, medium, and low populations were defined as the 75%–100%, 50%–75%, and 0%–25% of all mRuby2+ cells. HyperP and non-hyperP were defined as normal. The percentages of each subpopulation are shown in (C), with the percentages summing to 25% for each mRuby2 subpopulation by definition. Mean is shown with 95% confidence interval; marker style denotes biological replicates; n = 2–3 biological replicates per condition; two-tailed t test.

(D and E) Conversion outcome at 14 dpi for each of the sorted subpopulations in (B) and (C). (D) Diagram of model and (E) supporting conversion purities showing that proliferation history leads to different conversion rates based on TF expression early in conversion at 4 dpi. Mean is shown with 95% confidence interval; marker style denotes biological replicates; n = 2–3 biological replicates per condition (2 for mRuby2-low populations).

Significance summary: $p > 0.05$ (ns); *$p \leq 0.05$; **$p \leq 0.01$; ***$p \leq 0.001$; and ****$p \leq 0.0001$.

screening at scale. We hypothesized that differences in proliferation rates between MEFs and human fibroblasts may account for the difference in conversion yield. Further, given that hyperP MEFs convert at higher rates, we hypothesized that driving proliferation would be an effective way to increase conversion of human cells. Thus, we focused on increasing the proliferation rate of adult human fibroblasts by addition of genes known to drive proliferation.

Previously, for direct conversion of adult HDFs into motor neurons, we used a large conversion cocktail termed 7F (Brn2, Ascl1, Mytl1, Ngn2, Isl1, Lhx3, NeuroD1), which is the 6F cocktail with additional NeuroD1.[9,23] Based on our experience with mouse direct conversion, we reasoned that removing Brn2, which limits proliferation, and simplifying the conversion cocktail to our optimal, single-transcript motor neuron module (LNI, Lhx3-2A-Ngn2^{x3HA}-2A-Isl1; see Wang et al.[44]) would improve human fibroblast conversion (Figure 7A). Thus, we examined conversion with 7F or LNI cocktails in combination with several high-efficiency modules to boost proliferation. We quantified proliferation using a CellTrace dilution assay measured at 7 dpi and assessed conversion by staining cells for neural markers at 35 dpi (Figure 7B).

The inclusion of p53DD (DD) increases the total number and percentage of hyperP cells in the LNI condition (Figures 7C–7F). Previously, we observed that the inclusion of both p53DD and HRAS^{G12V} increased proliferation of mouse fibroblasts.[23] In contrast, we observed that the addition of HRAS^{G12V} to LNI + DD reduces hyperproliferation (Figures 7D and 7E). Given that HRAS^{G12V} was not effective in increasing the number of hyperP human fibroblasts, we looked for other factors that would drive proliferation. Oncogenes including myr-AKT, BCL2, and c-MYC (ABC) are known to drive proliferation in human epithelial cells,[48] thus we hypothesized that they could increase proliferation and conversion. Indeed, the addition of ABC to adult human fibroblasts resulted in a 2.6-fold increase in the number of hyperP cells co-transduced with LNI + DD (Figure 7D). Seeding densities can also influence proliferation rates. In the presence of DD + ABC, we observed that higher seeding densities increase the fraction and number of hyperP cells (Figures S6A–S6C). However, by microtubule-associated protein 2 (MAP2) and neuron-specific class III β-tubulin (TUJ1) staining at 35 dpi, we observed similarly dense and connected networks of morphologically mature neurons with LNI + DD + ABC across seeding densities (Figures S6D and S6E), suggesting that seeding density for human fibroblasts was not a strong determinant of neuron density at 35 dpi.

With an improved human-specific module to drive proliferation, we assessed neuron formation induced by the different cocktails by immunofluorescent staining for the neuronal markers TUJ1 and MAP2. In alignment with the increase in proliferation rates, the addition of ABC to the larger TF cocktail of 7F and the minimized cocktails of both LNI and NIL generates

Please cite this article in press as: Wang et al., Proliferation history and transcription factor levels drive direct conversion to motor neurons, Cell Systems (2025), https://doi.org/10.1016/j.cels.2025.101205

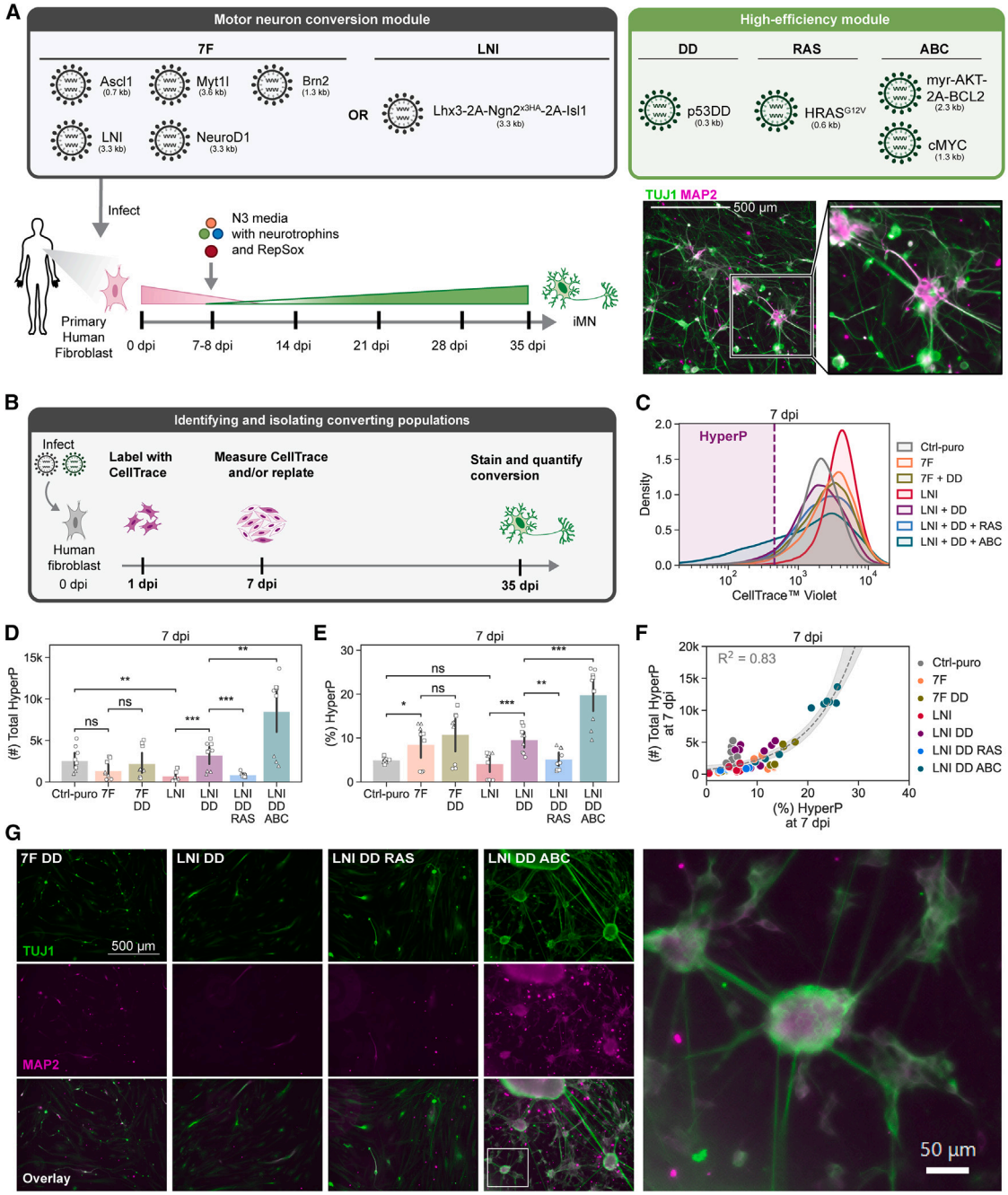

Figure 7. Driving hyperproliferation improves direct conversion of adult human fibroblasts

(A) Schematic depicting the conversion process for human dermal fibroblasts. Representative image shows cells converted with LNI DD ABC stained with TUJ1 and MAP2 at 35 dpi. Scale bar represents 500 µm in both image and enlarged inset.

(B) Schematic of the CellTrace dilution assay. HDFs are labeled 1 dpi, and their fluorescent intensity is measured at 7 dpi, where cells that have gone through many divisions have low fluorescence.

(C) Representative CellTrace distributions across conditions. Hyperproliferative cells are defined relative to the 5%-lowest fluorescent cells in a Ctrl-puro infection condition for a given biological replicate.

(D) HyperP percentage at 7 dpi across conditions. Ctrl-puro is 5% HyperP by definition. Mean is shown with 95% confidence interval; $n = 3$ biological replicates per condition; one-tailed t test with Bonferroni correction.

(E) HyperP total number at 7 dpi across conditions. Mean is shown with 95% confidence interval; $n = 3$ biological replicates per condition; one-tailed t test with Bonferroni correction.

(legend continued on next page)

Please cite this article in press as: Wang et al., Proliferation history and transcription factor levels drive direct conversion to motor neurons, Cell Systems (2025), https://doi.org/10.1016/j.cels.2025.101205

more TUJ1- and MAP2-positive cells (Figures 7G and S7A). Cells converted with the addition of ABC display mature, neuronal morphologies, and cultures form clusters of neurons with interconnecting neurites as observed for iPSC-derived neurons (Figures 7G, S7B, and S7C).[49,50] In contrast, cells converted without ABC exhibit MAP2 and TUJ1 staining but less neuronal morphologies. Overall, we observed species-specific responses in proliferation to different high-efficiency factors. By identifying an effective set of factors to increase hyperproliferation in adult human fibroblasts, we were able to increase human conversion efficiency through the axis of proliferation.

DISCUSSION

Despite improved techniques and tools, low conversion rates and diverse sources of extrinsic variation have limited our ability to interrogate and engineer cell-fate transitions. To reduce extrinsic variation and resolve the impact of TF levels on conversion, we tailored our motor neuron TF module to a minimal set of three factors (Ngn2, Isl1, Lhx3) and developed a single-transcript, high-efficiency module based on our previously developed chemo-genetic DDRR cocktail.[44] With the statistical power conferred by higher conversion rates, we identified how expression of individual TFs impacts conversion. Through systematic titration, we demonstrated that the efficiency of MEF-to-iMN direct conversion positively correlates with levels of the pioneer TF Ngn2 early in the conversion process and depends on the cell's proliferation history. We applied these observations to develop conversion cocktails that improve direct conversion rates in human cells.

While TFs drive cell-fate conversion, global processes such as transcription and proliferation can promote or impede expression of transgenic TFs. We set out to resolve how cells integrate contradictory cues from proliferation and TF expression during successful conversion events. We found that hyperP cells convert at higher rates despite reduced levels of transgene expression. Our results suggest that proliferation confers a state of receptivity to TFs factors. Once cells attain this proliferation-mediated state of receptivity, TF levels direct cells in distinct ways. High levels of the pioneer TF Ngn2 correlate to higher rates of conversion, whereas expression of Isl1 and Lhx3 do not show positive correlations early in conversion. One potential mechanism by which rapid proliferation may facilitate cell-fate transitions is through creating a more receptive chromatin landscape via replication. Post replication, nascent chromatin must re-establish steady-state accessibility.[51] Putatively, early opening of chromatin via pioneer activity of Ngn2 may provide accessibility to the other conversion TFs. Additionally, high rates of transcription in hyperP cells allow cells to convert at near-deterministic rates.[23] Potentially, Ngn2 levels may drive high rates of transcription in hyperP cells and enable cells to convert at high rates. Exploring the epigenetic profiles of hyperP cells during conversion may reveal features of chromatin that are receptive to TFs during direct cell-fate conversion.

By isolating the hyperP cells in our analyses, we could control for the effect of proliferation as a confounding factor on levels of TFs and for their influence on conversion from this privileged cell state. Specifically, we found that Brn2 alone strongly reduces proliferation and the number of neurons formed. Thus, Brn2 impedes cells' entry into a proliferation-mediated receptive state, making it difficult to decouple Brn2's neurogenic potential from its effects on proliferation. In contrast, Ascl1 can increase conversion without changing proliferation rates. Further, we showed that Ascl1 is dispensable for direct conversion of fibroblasts to motor neurons.[52–55] Eliminating Ascl1 from the conversion cocktail may also remove differences in conversion caused by distinct mechanistic pathways of the pro-neural, pioneering TFs, Ascl1, and Ngn2.[56,57] In addition, variation in Brn2 expression in 6F cocktails may potentially explain previously noted variability in conversion rates as well as observations by others that Brn2 cocktails rapidly drive cells to exit the cell cycle.[37,55] While other direct conversion cocktails to neural lineages report early cell-cycle exit,[53,58] we found that the more effective set of TFs (i.e., NIL) lengthens the period over which cells proliferate and convert. Notably, the TF-specific trends we observed in the hyperP population were diminished in the non- hyperP cells, obscuring the impact of individual TFs (Figure S4D). As hyperP cells often represent a small fraction of conversion cultures, trends observed in bulk populations may mask the processes that actually drive conversion within these highly convertible cells.

Conversion has been extensively studied through transcriptional profiling.[7,24,59–64] However, TFs activate gene regulatory networks as proteins. Posttranslational regulation of protein levels can generate large variance between levels of RNA and protein for the same gene.[26–28] Here, we do not rely on transcriptional profiling to make claims about how TF levels influence conversion events. Instead, we focused on measuring protein levels to examine how transgenic TFs influence conversion events. In our individual TF titration, we quantified the expression of the exogenous transgenes. While the total levels of TFs may influence conversion, the exogenous factors represent the primary species that drive cell-fate transitions.

Collectively, our results show that proliferation history and TF expression combine to drive cell-fate transitions. We find that although hyperP cells express lower levels of conversion TFs, proliferation-mediated receptivity enables them to convert at higher rates. Thus, control of TF levels alone is not sufficient to precisely control cell fate. By developing tools that more precisely perturb multiple aspects of the conversion process, we will improve our understanding and control of cellular conversion. In this study, we primarily use oncogenes as strong drivers of proliferation to improve direct conversion to mouse and human motor neurons. Although we observed that cells can still efficiently convert to post-mitotic cell fates even in the presence of powerful oncogenes, clinical applications may require agents

(F) HyperP total number vs. percentage at 7 dpi across all conversion conditions. An exponential fit is shown with 95% confidence interval.
(G) Representative images at 35 dpi of cells fixed and stained with TUJ1 and MAP2 with a seeding density of 2,500 cells per 96-well. Scale bar represents 500 μm in images and 50 μm in the enlarged inset on the right.
Significance summary: $p > 0.05$ (ns); *$p \leq 0.05$; **$p \leq 0.01$; ***$p \leq 0.001$; and ****$p \leq 0.0001$.

with a higher safety profile to drive proliferation. Potentially, permanent integration of oncogenes can be replaced with transient transgene delivery, excision of the high-efficiency module, or small-molecule replacements.[65] Beyond targeting conversion to specific cell types, precise control of transgenes to induce conversion of human cells will improve safety and efficacy of gene and cell-based therapies for regeneration of neural tissue.

RESOURCE AVAILABILITY

Lead contact

Requests for further information and resources should be directed to and will be fulfilled by the lead contact, Kate E. Galloway, PhD (katiegal@mit.edu).

Materials availability

Plasmids generated in this study have been deposited to Addgene.

Data and code availability

- Data have been deposited at Zenodo: https://doi.org/10.5281/zenodo.14743917.
- Code is available at https://github.com/GallowayLabMIT/article-prolif-TF-levels. The DOI is listed in the key resources table.
- Any additional information required to reanalyze the data reported in this paper is available from the lead contact upon request.

ACKNOWLEDGMENTS

Research reported in this manuscript was supported by the National Institute of General Medical Sciences of the National Institutes of Health under award number R35-GM143033. A.M.B., B.A.L.-D., and N.B.W. are supported by the National Science Foundation Graduate Research Fellowship Program under grant no. 1745302. A.M.B. is also supported by the National Cancer Institute under award number F99CA284280. We thank the Koch Institute's Robert A. Swanson (1969) Biotechnology Center (National Cancer Institute grant P30-CA14051) for technical support, specifically the Flow Cytometry Core Facility. We thank Doug Lauffenberger and Christopher Johnstone, Sneha Kabaria, Emma Peterman, Deon Ploessl, Joji Teves, Mary Ehmann, and especially Kasey Love for feedback on the development of the manuscript.

AUTHOR CONTRIBUTIONS

N.B.W., A.M.B., and B.A.L.-D. performed and analyzed mouse conversion. B.A.L.-D., A.M.B., and P.H. performed and analyzed human conversion. K.E.G. and T.M.O. supervised the project. N.B.W., K.E.G., B.A.L.-D., H.O.A., and T.M.O. wrote the manuscript.

DECLARATION OF INTERESTS

The authors declare no competing interests.

STAR★METHODS

Detailed methods are provided in the online version of this paper and include the following:

- KEY RESOURCES TABLE
- EXPERIMENTAL MODEL AND STUDY PARTICIPANT DETAILS
  - Cell lines and tissue culture
  - MEF dissection and isolation
- METHOD DETAILS
  - Plasmid construction
  - Viral transduction and iMN conversion of MEFs
  - Quantification of conversion yield, purity, and efficiency
  - CellTrace labeling to measure cellular proliferation
  - Flow cytometry and FACS
  - Fixation and immunofluorescent staining
  - Morphology quantification of Hb9::GFP-positive cells
  - 5-ethynyl-2'-deoxyuridine (EdU) assay to detect cell cycle progression
  - Brn2-2A-mRuby2 multiplicity of infection (MOI) calculation and conversion assay
  - Twin conversion assays for 4 dpi exogenous transgene reporter and 14 dpi conversion
  - Ngn2-2A-mRuby2 and proliferation history dual sort
  - Viral transduction and iMN conversion of human adult dermal fibroblasts
  - Morphology quantification of human iMNs
  - Fluorescent imaging
- QUANTIFICATION AND STATISTICAL ANALYSIS

SUPPLEMENTAL INFORMATION

Supplemental information can be found online at https://doi.org/10.1016/j.cels.2025.101205.

Received: December 28, 2023
Revised: November 7, 2024
Accepted: February 11, 2025
Published: March 13, 2025

REFERENCES

1. Shakiba, N., Fahmy, A., Jayakumaran, G., McGibbon, S., David, L., Trcka, D., Elbaz, J., Puri, M.C., Nagy, A., van der Kooy, D., et al. (2019). Cell competition during reprogramming gives rise to dominant clones. Science *364*, eaan0925. https://doi.org/10.1126/science.aan0925.
2. Yamanaka, S. (2009). Elite and stochastic models for induced pluripotent stem cell generation. Nature *460*, 49–52. https://doi.org/10.1038/nature08180.
3. Chen, S.-W., Hung, Y.-S., Fuh, J.-L., Chen, N.-J., Chu, Y.-S., Chen, S.-C., Fann, M.-J., and Wong, Y.-H. (2021). Efficient conversion of human induced pluripotent stem cells into microglia by defined transcription factors. Stem Cell Rep. *16*, 1363–1380. https://doi.org/10.1016/j.stemcr.2021.03.010.
4. Feng, R., Desbordes, S.C., Xie, H., Tillo, E.S., Pixley, F., Stanley, E.R., and Graf, T. (2008). PU.1 and C/EBPalpha/beta convert fibroblasts into macrophage-like cells. Proc. Natl. Acad. Sci. USA *105*, 6057–6062. https://doi.org/10.1073/pnas.0711961105.
5. Ieda, M., Fu, J.-D., Delgado-Olguin, P., Vedantham, V., Hayashi, Y., Bruneau, B.G., and Srivastava, D. (2010). Direct reprogramming of fibroblasts into functional cardiomyocytes by defined factors. Cell *142*, 375–386. https://doi.org/10.1016/j.cell.2010.07.002.
6. Lujan, E., Chanda, S., Ahlenius, H., Südhof, T.C., and Wernig, M. (2012). Direct conversion of mouse fibroblasts to self-renewing, tripotent neural precursor cells. Proc. Natl. Acad. Sci. USA *109*, 2527–2532. https://doi.org/10.1073/pnas.1121003109.
7. Mall, M., Kareta, M.S., Chanda, S., Ahlenius, H., Perotti, N., Zhou, B., Grieder, S.D., Ge, X., Drake, S., Euong Ang, C., et al. (2017). Myt1l safeguards neuronal identity by actively repressing many non-neuronal fates. Nature *544*, 245–249. https://doi.org/10.1038/nature21722.
8. Rosa, F.F., Pires, C.F., Kurochkin, I., Ferreira, A.G., Gomes, A.M., Palma, L.G., Shaiv, K., Solanas, L., Azenha, C., Papatsenko, D., et al. (2018). Direct reprogramming of fibroblasts into antigen-presenting dendritic cells. Sci. Immunol. *3*, eaau4292. https://doi.org/10.1126/sciimmunol.aau4292.
9. Son, E.Y., Ichida, J.K., Wainger, B.J., Toma, J.S., Rafuse, V.F., Woolf, C.J., and Eggan, K. (2011). Conversion of mouse and human fibroblasts into functional spinal motor neurons. Cell Stem Cell *9*, 205–218. https://doi.org/10.1016/j.stem.2011.07.014.
10. Soufi, A., Garcia, M.F., Jaroszewicz, A., Osman, N., Pellegrini, M., and Zaret, K.S. (2015). Pioneer transcription factors target partial DNA motifs

on nucleosomes to initiate reprogramming. Cell *161*, 555–568. https://doi.org/10.1016/j.cell.2015.03.017.

11. Soufi, A., Donahue, G., and Zaret, K.S. (2012). Facilitators and impediments of the pluripotency reprogramming factors' initial engagement with the genome. Cell *151*, 994–1004. https://doi.org/10.1016/j.cell.2012.09.045.
12. Sridharan, R., Tchieu, J., Mason, M.J., Yachechko, R., Kuoy, E., Horvath, S., Zhou, Q., and Plath, K. (2009). Role of the murine reprogramming factors in the induction of pluripotency. Cell *136*, 364–377. https://doi.org/10.1016/j.cell.2009.01.001.
13. Takahashi, K., and Yamanaka, S. (2006). Induction of pluripotent stem cells from mouse embryonic and adult fibroblast cultures by defined factors. Cell *126*, 663–676. https://doi.org/10.1016/j.cell.2006.07.024.
14. Velychko, S., Adachi, K., Kim, K.-P., Hou, Y., MacCarthy, C.M., Wu, G., and Schöler, H.R. (2019). Excluding Oct4 from Yamanaka cocktail unleashes the developmental potential of iPSCs. Cell Stem Cell *25*, 737–753.e4. https://doi.org/10.1016/j.stem.2019.10.002.
15. Wang, L., Liu, Z., Yin, C., Asfour, H., Chen, O., Li, Y., Bursac, N., Liu, J., and Qian, L. (2015). Stoichiometry of Gata4, Mef2c, and Tbx5 influences the efficiency and quality of induced cardiac myocyte reprogramming. Circ. Res. *116*, 237–244. https://doi.org/10.1161/CIRCRESAHA.116.305547.
16. Wernig, M., Meissner, A., Cassady, J.P., and Jaenisch, R. (2008). c-Myc Is Dispensable for Direct Reprogramming of Mouse Fibroblasts. Cell Stem Cell *2*, 10–12. https://doi.org/10.1016/j.stem.2007.12.001.
17. An, Z., Liu, P., Zheng, J., Si, C., Li, T., Chen, Y., Ma, T., Zhang, M.Q., Zhou, Q., and Ding, S. (2019). Sox2 and Klf4 as the functional core in pluripotency induction without exogenous Oct4. Cell Rep. *29*, 1986–2000.e8. https://doi.org/10.1016/j.celrep.2019.10.026.
18. Carey, B.W., Markoulaki, S., Hanna, J.H., Faddah, D.A., Buganim, Y., Kim, J., Ganz, K., Steine, E.J., Cassady, J.P., Creyghton, M.P., et al. (2011). Reprogramming factor stoichiometry influences the epigenetic state and biological properties of induced pluripotent stem cells. Cell Stem Cell *9*, 588–598. https://doi.org/10.1016/j.stem.2011.11.003.
19. Kempf, J., Knelles, K., Hersbach, B.A., Petrik, D., Riedemann, T., Bednarova, V., Janjic, A., Simon-Ebert, T., Enard, W., Smialowski, P., et al. (2021). Heterogeneity of neurons reprogrammed from spinal cord astrocytes by the proneural factors Ascl1 and neurogenin2. Cell Rep. *36*, 109409. https://doi.org/10.1016/j.celrep.2021.109409.
20. Jain, N., Goyal, Y., Dunagin, M.C., Cote, C.J., Mellis, I.A., Emert, B., Jiang, C.L., Dardani, I.P., Reffsin, S., Arnett, M., et al. (2024). Retrospective identification of cell-intrinsic factors that mark pluripotency potential in rare somatic cells. Cell Syst. *15*, 109–133.e10. https://doi.org/10.1016/j.cels.2024.01.001.
21. Wang, N.B., Beitz, A.M., and Galloway, K.E. (2020). Engineering cell fate: applying synthetic biology to cellular reprogramming. Curr. Opin. Syst. Biol. *24*, 18–31. https://doi.org/10.1016/j.coisb.2020.09.002.
22. Ilia, K., Shakiba, N., Bingham, T., Jones, R.D., Kaminski, M.M., Aravera, E., Bruno, S., Palacios, S., Weiss, R., Collins, J.J., et al. (2023). Synthetic genetic circuits to uncover the OCT4 trajectories of successful reprogramming of human fibroblasts. Sci. Adv. *9*, eadg8495. https://doi.org/10.1126/sciadv.adg8495.
23. Babos, K.N., Galloway, K.E., Kisler, K., Zitting, M., Li, Y., Shi, Y., Quintino, B., Chow, R.H., Zlokovic, B.V., and Ichida, J.K. (2019). Mitigating antagonism between transcription and proliferation allows near-deterministic cellular reprogramming. Cell Stem Cell *25*, 486–500.e9. https://doi.org/10.1016/j.stem.2019.08.005.
24. Jindal, K., Adil, M.T., Yamaguchi, N., Yang, X., Wang, H.C., Kamimoto, K., Rivera-Gonzalez, G.C., and Morris, S.A. (2023). Single-cell lineage capture across genomic modalities with CellTag-multi reveals fate-specific gene regulatory changes. Nat. Biotechnol. *42*, 946–959. https://doi.org/10.1038/s41587-023-01931-4.
25. Hersbach, B.A., Fischer, D.S., Masserdotti, G., Deeksha, M., Mojžišová, K., Waltzhöni, T., Rodriguez-Terrones, D., Heinig, M., Theis, F.J., Götz, M., et al. (2022). Probing cell identity hierarchies by fate titration and collision during direct reprogramming. Mol. Syst. Biol. *18*, e11129. https://doi.org/10.15252/msb.202211129.
26. Hafner, A., Stewart-Ornstein, J., Purvis, J.E., Forrester, W.C., Bulyk, M.L., and Lahav, G. (2017). p53 pulses lead to distinct patterns of gene expression albeit similar DNA-binding dynamics. Nat. Struct. Mol. Biol. *24*, 840–847. https://doi.org/10.1038/nsmb.3452.
27. Ideker, T., Thorsson, V., Ranish, J.A., Christmas, R., Buhler, J., Eng, J.K., Bumgarner, R., Goodlett, D.R., Aebersold, R., and Hood, L. (2001). Integrated genomic and proteomic analyses of a systematically perturbed metabolic network. Science *292*, 929–934. https://doi.org/10.1126/science.292.5518.929.
28. Lundberg, E., Fagerberg, L., Klevebring, D., Matic, I., Geiger, T., Cox, J., Älgenäs, C., Lundeberg, J., Mann, M., and Uhlen, M. (2010). Defining the transcriptome and proteome in three functionally different human cell lines. Mol. Syst. Biol. *6*, 450. https://doi.org/10.1038/msb.2010.106.
29. Hu, X., Wu, Q., Zhang, J., Chen, X., Hartman, A., Eastman, A., and Guo, S. (2020). Reprogramming progressive cells display low CAG promoter activity. Preprint at bioRxiv. https://doi.org/10.1101/2020.03.03.975664.
30. Kueh, H.Y., Champhekar, A., Nutt, S.L., Elowitz, M.B., and Rothenberg, E.V. (2013). Positive feedback between PU.1 and the cell cycle controls myeloid differentiation. Science *341*, 670–673. https://doi.org/10.1126/science.1240831.
31. Palozola, K.C., Donahue, G., Liu, H., Grant, G.R., Becker, J.S., Cote, A., Yu, H., Raj, A., and Zaret, K.S. (2017). Mitotic transcription and waves of gene reactivation during mitotic exit. Science *358*, 119–122. https://doi.org/10.1126/science.aal4671.
32. Percharde, M., Bulut-Karslioglu, A., and Ramalho-Santos, M. (2017). Hypertranscription in development, stem cells, and regeneration. Dev. Cell *40*, 9–21. https://doi.org/10.1016/j.devcel.2016.11.010.
33. Stadhouders, R., Vidal, E., Serra, F., Di Stefano, B., Le Dily, F., Quilez, J., Gomez, A., Collombet, S., Berenguer, C., Cuartero, Y., et al. (2018). Transcription factors orchestrate dynamic interplay between genome topology and gene regulation during cell reprogramming. Nat. Genet. *50*, 238–249. https://doi.org/10.1038/s41588-017-0030-7.
34. Bowman, S.K., Rolland, V., Betschinger, J., Kinsey, K.A., Emery, G., and Knoblich, J.A. (2008). The tumor suppressors brat and Numb regulate transit-amplifying neuroblast lineages in Drosophila. Dev. Cell *14*, 535–546. https://doi.org/10.1016/j.devcel.2008.03.004.
35. Bultje, R.S., Castaneda-Castellanos, D.R., Jan, L.Y., Jan, Y.-N., Kriegstein, A.R., and Shi, S.-H. (2009). Mammalian Par3 regulates progenitor cell asymmetric division via Notch signaling in the developing neocortex. Neuron *63*, 189–202. https://doi.org/10.1016/j.neuron.2009.07.004.
36. Eriksson, P.S., Perfilieva, E., Björk-Eriksson, T., Alborn, A.M., Nordborg, C., Peterson, D.A., and Gage, F.H. (1998). Neurogenesis in the adult human hippocampus. Nat. Med. *4*, 1313–1317. https://doi.org/10.1038/3305.
37. Vierbuchen, T., Ostermeier, A., Pang, Z.P., Kokubu, Y., Südhof, T.C., and Wernig, M. (2010). Direct conversion of fibroblasts to functional neurons by defined factors. Nature *463*, 1035–1041. https://doi.org/10.1038/nature08797.
38. Di Tullio, A., and Graf, T. (2012). C/EBPα bypasses cell cycle-dependency during immune cell transdifferentiation. Cell Cycle *11*, 2739–2746. https://doi.org/10.4161/cc.21119.
39. Fishman, V.S., Shnayder, T.A., Orishchenko, K.E., Bader, M., Alenina, N., and Serov, O.L. (2015). Cell divisions are not essential for the direct conversion of fibroblasts into neuronal cells. Cell Cycle *14*, 1188–1196. https://doi.org/10.1080/15384101.2015.1012875.
40. Heinrich, C., Blum, R., Gascón, S., Masserdotti, G., Tripathi, P., Sánchez, R., Tiedt, S., Schroeder, T., Götz, M., and Berninger, B. (2010). Directing astroglia from the cerebral cortex into subtype specific functional neurons. PLoS Biol. *8*, e1000373. https://doi.org/10.1371/journal.pbio.1000373.
41. Guo, S., Zi, X., Schulz, V.P., Cheng, J., Zhong, M., Koochaki, S.H.J., Megyola, C.M., Pan, X., Heydari, K., Weissman, S.M., et al. (2014).

Nonstochastic reprogramming from a privileged somatic cell state. Cell *156*, 649–662. https://doi.org/10.1016/j.cell.2014.01.020.

42. Hanna, J., Saha, K., Pando, B., van Zon, J., Lengner, C.J., Creyghton, M.P., van Oudenaarden, A., and Jaenisch, R. (2009). Direct cell reprogramming is a stochastic process amenable to acceleration. Nature *462*, 595–601. https://doi.org/10.1038/nature08592.
43. Wichterle, H., Lieberam, I., Porter, J.A., and Jessell, T.M. (2002). Directed differentiation of embryonic stem cells into motor neurons. Cell *110*, 385–397. https://doi.org/10.1016/S0092-8674(02)00835-8.
44. Wang, N.B., Adewumi, H.O., Lende-Dorn, B.A., Beitz, A.M., O'Shea, T.M., and Galloway, K.E. (2025). Compact transcription factor cassettes generate functional, engraftable motor neurons by direct conversion. Cell Syst. 16. https://doi.org/10.1016/j.cels.2025.101206.
45. Mazzoni, E.O., Mahony, S., Closser, M., Morrison, C.A., Nedelec, S., Williams, D.J., An, D., Gifford, D.K., and Wichterle, H. (2013). Synergistic binding of transcription factors to cell-specific enhancers programs motor neuron identity. Nat. Neurosci. *16*, 1219–1227. https://doi.org/10.1038/nn.3467.
46. Ferreira, J.P., Overton, K.W., and Wang, C.L. (2013). Tuning gene expression with synthetic upstream open reading frames. Proc. Natl. Acad. Sci. USA *110*, 11284–11289. https://doi.org/10.1073/pnas.1305590110.
47. Jones, R.D., Qian, Y., Siciliano, V., DiAndreth, B., Huh, J., Weiss, R., and Del Vecchio, D. (2020). An endoribonuclease-based feedforward controller for decoupling resource-limited genetic modules in mammalian cells. Nat. Commun. *11*, 5690. https://doi.org/10.1038/s41467-020-19126-9.
48. Park, J.W., Lee, J.K., Sheu, K.M., Wang, L., Balanis, N.G., Nguyen, K., Smith, B.A., Cheng, C., Tsai, B.L., Cheng, D., et al. (2018). Reprogramming normal human epithelial tissues to a common, lethal neuroendocrine cancer lineage. Science *362*, 91–95. https://doi.org/10.1126/science.aat5749.
49. Álvarez, Z., Ortega, J.A., Sato, K., Sasselli, I.R., Kolberg-Edelbrock, A.N., Qiu, R., Marshall, K.A., Nguyen, T.P., Smith, C.S., Quinlan, K.A., et al. (2023). Artificial extracellular matrix scaffolds of mobile molecules enhance maturation of human stem cell-derived neurons. Cell Stem Cell *30*, 219–238.e14. https://doi.org/10.1016/j.stem.2022.12.010.
50. Blanch-Asensio, A., Ploessl, D.S., Wang, N.B., Mummery, C.L., Galloway, K.E., and Davis, R.P. (2024). STRAIGHT-IN Dual: a platform for dual, single-copy integrations of DNA payloads and gene circuits into human induced pluripotent stem cells. Preprint at bioRxiv. https://doi.org/10.1101/2024.10.17.616637.
51. Stewart-Morgan, K.R., Reverón-Gómez, N., and Groth, A. (2019). Transcription restart establishes chromatin accessibility after DNA replication. Mol. Cell *75*, 284–297.e6. https://doi.org/10.1016/j.molcel.2019.04.033.
52. Chanda, S., Ang, C.E., Davila, J., Pak, C., Mall, M., Lee, Q.Y., Ahlenius, H., Jung, S.W., Südhof, T.C., and Wernig, M. (2014). Generation of induced neuronal cells by the single reprogramming factor ASCL1. Stem Cell Rep. *3*, 282–296. https://doi.org/10.1016/j.stemcr.2014.05.020.
53. Treutlein, B., Lee, Q.Y., Camp, J.G., Mall, M., Koh, W., Shariati, S.A.M., Sim, S., Neff, N.F., Skotheim, J.M., Wernig, M., et al. (2016). Dissecting direct reprogramming from fibroblast to neuron using single-cell RNA-seq. Nature *534*, 391–395. https://doi.org/10.1038/nature18323.
54. Wang, H., Yang, Y., Liu, J., and Qian, L. (2021). Direct cell reprogramming: approaches, mechanisms and progress. Nat. Rev. Mol. Cell Biol. *22*, 410–424. https://doi.org/10.1038/s41580-021-00335-z.
55. Wapinski, O.L., Vierbuchen, T., Qu, K., Lee, Q.Y., Chanda, S., Fuentes, D.R., Giresi, P.G., Ng, Y.H., Marro, S., Neff, N.F., et al. (2013). Hierarchical mechanisms for direct reprogramming of fibroblasts to neurons. Cell *155*, 621–635. https://doi.org/10.1016/j.cell.2013.09.028.
56. Aydin, B., Kakumanu, A., Rossillo, M., Moreno-Estellés, M., Garipler, G., Ringstad, N., Flames, N., Mahony, S., and Mazzoni, E.O. (2019). Proneural factors Ascl1 and Neurog2 contribute to neuronal subtype identities by establishing distinct chromatin landscapes. Nat. Neurosci. *22*, 897–908. https://doi.org/10.1038/s41593-019-0399-y.
57. Vainorius, G., Novatchkova, M., Michlits, G., Baar, J.C., Raupach, C., Lee, J., Yelagandula, R., Wernig, M., and Elling, U. (2023). Ascl1 and Ngn2 convert mouse embryonic stem cells to neurons via functionally distinct paths. Nat. Commun. *14*, 5341. https://doi.org/10.1038/s41467-023-40803-y.
58. Yoo, A.S., Sun, A.X., Li, L., Shcheglovitov, A., Portmann, T., Li, Y., Lee-Messer, C., Dolmetsch, R.E., Tsien, R.W., and Crabtree, G.R. (2011). MicroRNA-mediated conversion of human fibroblasts to neurons. Nature *476*, 228–231. https://doi.org/10.1038/nature10323.
59. Cahan, P., Li, H., Morris, S.A., Lummertz da Rocha, E.L., Daley, G.Q., and Collins, J.J. (2014). CellNet: network biology applied to stem cell engineering. Cell *158*, 903–915. https://doi.org/10.1016/j.cell.2014.07.020.
60. Cates, K., McCoy, M.J., Kwon, J.-S., Liu, Y., Abernathy, D.G., Zhang, B., Liu, S., Gontarz, P., Kim, W.K., Chen, S., et al. (2021). Deconstructing stepwise fate conversion of human fibroblasts to neurons by microRNAs. Cell Stem Cell *28*, 127–140.e9. https://doi.org/10.1016/j.stem.2020.08.015.
61. Nair, S., Ameen, M., Sundaram, L., Pampari, A., Schreiber, J., Balsubramani, A., Wang, Y.X., Burns, D., Blau, H.M., Karakikes, I., et al. (2023). Transcription factor stoichiometry, motif affinity and syntax regulate single-cell chromatin dynamics during fibroblast reprogramming to pluripotency. Preprint at bioRxiv. https://doi.org/10.1101/2023.10.04.560808.
62. Schiebinger, G., Shu, J., Tabaka, M., Cleary, B., Subramanian, V., Solomon, A., Gould, J., Liu, S., Lin, S., Berube, P., et al. (2019). Optimal-transport analysis of single-cell gene expression identifies developmental trajectories in reprogramming. Cell *176*, 928–943.e22. https://doi.org/10.1016/j.cell.2019.01.006.
63. Zhao, T., Fu, Y., Zhu, J., Liu, Y., Zhang, Q., Yi, Z., Chen, S., Jiao, Z., Xu, X., Xu, J., et al. (2018). Single-cell RNA-seq reveals dynamic early embryonic-like programs during chemical reprogramming. Cell Stem Cell *23*, 31–45.e7. https://doi.org/10.1016/j.stem.2018.05.025.
64. Zviran, A., Mor, N., Rais, Y., Gingold, H., Peles, S., Chomsky, E., Viukov, S., Buenrostro, J.D., Scognamiglio, R., Weinberger, L., et al. (2019). Deterministic somatic cell reprogramming involves continuous transcriptional changes governed by Myc and epigenetic-driven modules. Cell Stem Cell *24*, 328–341.e9. https://doi.org/10.1016/j.stem.2018.11.014.
65. Liuyang, S., Wang, G., Wang, Y., He, H., Lyu, Y., Cheng, L., Yang, Z., Guan, J., Fu, Y., Zhu, J., et al. (2023). Highly efficient and rapid generation of human pluripotent stem cells by chemical reprogramming. Cell Stem Cell *30*, 450–459.e9. https://doi.org/10.1016/j.stem.2023.02.008.

Please cite this article in press as: Wang et al., Proliferation history and transcription factor levels drive direct conversion to motor neurons, Cell Systems (2025), https://doi.org/10.1016/j.cels.2025.101205

STAR★METHODS

KEY RESOURCES TABLE

REAGENT or RESOURCE	SOURCE	IDENTIFIER
Antibodies		
rabbit anti-Ki67	GeneTex	Cat#GTX1667; RRID:AB_422351
mouse anti-TUBB3	Biolegend	Cat#801202; RRID:AB_10063408
rabbit anti-MAP2	Cell Signaling Technology	Cat##4542; RRID:AB_10693782
donkey anti-mouse Alexa Fluor 647	Invitrogen	Cat#A-31571; RRID: AB_162542
donkey anti-rabbit Alexa Fluor 594	Invitrogen	Cat#A-21207; RRID: AB_141637
donkey anti-rabbit Alexa Fluor 647	Invitrogen	Cat#A-31573; RRID:AB_2536183
goat anti-mouse Alexa Fluor 488	Jackson ImmunoResearch Labs	Cat#115-546-146; RRID:AB_2338868
Chemicals, peptides, and recombinant proteins		
RepSox (TGF-β inhibitor)	Selleck Chemicals	Cat#S7223
Recombinant Human BDNF Protein	R&D Systems	Cat#248-BDB-050
Recombinant Human CNTF Protein	R&D Systems	Cat#257-NT-050
Recombinant Human GDNF Protein	R&D Systems	Cat#212-GD-050
Recombinant Human Protein FGF-Basic (154 a.a.)	Peprotech	Cat#100-18B
(+)-Aphidicolin	Cayman Chemicals	Cat#38966-21-1
DAPI	Tocris	Cat#5748
DMEM	Genesee Scientific	Cat#25-500
Fetal Bovine Serum	Genesee Scientific	Cat#25-514H
HEPES	Sigma-Aldrich	Cat#H3375
Hexadimethrine bromide	Sigma-Aldrich	Cat#H9268
DMEM/F-12, no glutamine	Thermo Scientific	Cat#21-331-020
B-27 Supplement (50X), serum free	Thermo Scientific	Cat#17-504-044
N-2 Supplement (100X)	Thermo Scientific	Cat#17-502-048
GlutaMAX Supplement	Thermo Scientific	Cat#35-050-061
MEM Non Essential Amino Acids Solution (100X)	Thermo Scientific	Cat#11-140-050
DNase	Worthington Biochemical	Cat#9003-98-9
Papain	Worthington Biochemical	Cat#9001-73-4
Penicillin-Streptomycin (10,000 U/mL)	Thermo Scientific	Cat#15-140-122
Bovine Serum Albumin	Sigma-Aldrich	Cat#A2058
Laminin	Corning	Cat#354232
Gelatin	Sigma-Aldrich	Cat#G1890
Lenti-X Concentrator	Takara Bio	Cat#631232
Critical commercial assays		
CellTrace Violet Cell Proliferation Kit, for flow cytometry	Thermo Scientific	Cat#C34557
CellTrace Far Red Cell Proliferation Kit, for flow cytometry	Thermo Scientific	Cat#C34564
Click-iT Plus EdU Alexa Fluor 647 Flow Cytometry Assay Kit	Thermo Scientific	Cat#C10635
Deposited data		
Raw and analyzed data	This study	Zenodo: https://doi.org/10.5281/zenodo.14743917

(*Continued on next page*)

Continued

REAGENT or RESOURCE	SOURCE	IDENTIFIER
Experimental models: Cell lines		
Human: Fibroblast from Skin (Female, 44YR)	Coriell Institute	Cat#GM05116
Human: HEK293T	ATCC	Cat#CRL-3216
Human: Plat-E Retroviral Packaging Cell Line	Cell Biolabs, Inc.	Cat#RV-101
Experimental models: Organisms/strains		
Mouse: C57BL/6J	The Jackson Laboratory	Cat#000664, RRID:IMSR_JAX:000664
Mouse: B6.Cg-Tg(Hlxb9-GFP)1Tmj/J	The Jackson Laboratory	Cat#005029, RRID:IMSR_JAX:005029
Recombinant DNA		
pMXs-mNgn2	This study	Addgene #233148
pMXs-Isl1	This study	Addgene #233149
pMXs-mLhx3	This study	Addgene #233150
pMXs-mBrn2	This study	Addgene #233151
pMXs-mAscl1	This study	Addgene #233152
pMXs-hMyt1l	This study	Addgene #233153
pMXs-NIL	This study	Addgene #233154
pMXs-HRAS(G12V)-IRES-p53DD	This study	Addgene #233185
pMXs-mRuby2	This study	Addgene #233155
pMXs-mBrn2-P2A-mRuby2	This study	Addgene #233156
pENTR-mNgn2x3HA-P2A-mRuby2	This study	Addgene #233157
pENTR-Isl1-P2A-mRuby2	This study	Addgene #233158
pENTR-mLhx3-P2A-mRuby2	This study	Addgene #233159
pMXs-Isl1-T2A-mLhx3	This study	Addgene #233160
pMXs-mNgn2x3HA-T2A-Isl1	This study	Addgene #233161
pMXs-mNgn2x3HA-T2A-mLhx3	This study	Addgene #233162
pMXs-mNgn2x3HA-P2A-mRuby2	This study	Addgene #233163
pMXs-uORFwx1-mNgn2x3HA-P2A-mRuby2	This study	Addgene #233164
pMXs-uORFx1-mNgn2x3HA-P2A-mRuby2	This study	Addgene #233165
pMXs-uORFx2-mNgn2x3HA-P2A-mRuby2	This study	Addgene #233166
pMXs-uORFx3-mNgn2x3HA-P2A-mRuby2	This study	Addgene #233167
pMXs-uORFx6-mNgn2x3HA-P2A-mRuby2	This study	Addgene #233168
pMXs-Isl1-P2A-mRuby2	This study	Addgene #233169
pMXs-uORFwx1-Isl1-P2A-mRuby2	This study	Addgene #233170
pMXs-uORFx1-Isl1-P2A-mRuby2	This study	Addgene #233171
pMXs-uORFx2-Isl1-P2A-mRuby2	This study	Addgene #233172
pMXs-uORFx3-Isl1-P2A-mRuby2	This study	Addgene #233173
pMXs-uORFx6-Isl1-P2A-mRuby2	This study	Addgene #233174
pMXs-mLhx3-P2A-mRuby2	This study	Addgene #233175
pMXs-uORFwx1-mLhx3-P2A-mRuby2	This study	Addgene #233176
pMXs-uORFx1-mLhx3-P2A-mRuby2	This study	Addgene #233177
pMXs-uORFx2-mLhx3-P2A-mRuby2	This study	Addgene #233178
pMXs-uORFx3-mLhx3-P2A-mRuby2	This study	Addgene #233179
pMXs-uORFx6-mLhx3-P2A-mRuby2	This study	Addgene #233180
pMXs-p53DD	Addgene	Addgene #22729
pMXs-HRAS(GV12)	This study	Addgene #233181
pMXs-myrAkt-P2A-BCL2	This study	Addgene #233182
pMXs-cMyc	This study	Addgene #233183
pMXs-hNeuroD1	This study	Addgene #233184

(*Continued on next page*)

Please cite this article in press as: Wang et al., Proliferation history and transcription factor levels drive direct conversion to motor neurons, Cell Systems (2025), https://doi.org/10.1016/j.cels.2025.101205

Continued

REAGENT or RESOURCE	SOURCE	IDENTIFIER
Software and algorithms		
Code	This study	https://doi.org/10.5281/zenodo.14851683
Adobe Illustrator CC	Adobe Systems	https://www.adobe.com
Python 3	N/A	https://www.python.org
ImageJ	N/A	https://imagej.net
FlowJo	N/A	https://www.flowjo.com/

EXPERIMENTAL MODEL AND STUDY PARTICIPANT DETAILS

Cell lines and tissue culture

HEK293T, Plat-E, and mouse embryonic fibroblasts were cultured in DMEM supplemented with 10% FBS at 37°C, 5% CO_2. Plat-E cells were selected using 10 μg/mL blastocidin and 1 μg/mL puromycin every three passages. Human adult dermal fibroblasts were cultured in DMEM supplemented with 15% FBS and non-essential amino acids at 37°C, 5% CO_2. The following are sex of primary human fibroblasts used in this study: female (GM05116). Cultures were periodically tested for mycoplasma.

MEF dissection and isolation

C57BL/6 mice were mated with mice bearing the Hb9::GFP reporter. Mouse embryonic fibroblasts were isolated at E12.5-E14.5 under a dissection microscope. Embryos were sorted into non-transgenic and Hb9::GFP+ by using a blue laser to illuminate the spinal cord to identify the presence of Hb9::GFP+ cells. After removing the head and internal organs to avoid contaminating neurons and other cells, razors were used to break up the tissue for 5 minutes in the presence of 0.25% Trypsin-EDTA. Up to two embryos were processed at the same time. The preliminary suspension was neutralized, resuspended, and triturated with 0.25% Trypsin-EDTA. Again, the suspension was neutralized, resuspended, and filtered through a 40 μm cell strainer. MEF cultures were expanded on 0.1% gelatin coated 10 cm dishes, using one 10 cm dish per embryo. MEFs were expanded until ~80% confluent, passaged, and expanded for at least 3-4 days. Passage 1 MEFs were tested for mycoplasma, cryopreserved in 90% FBS and 10% DMSO, and kept in liquid nitrogen.

METHOD DETAILS

Plasmid construction

Entry vectors were constructed by Gibson and Golden gate cloning. Retroviral vectors were constructed by Gateway cloning into pMXs-WPRE-DEST using an LR reaction, respectively. Viral plasmids were confirmed via Sanger or whole plasmid sequencing. For a complete list of plasmids, see supplementary files, including Data S1 and Table S1.

Viral transduction and iMN conversion of MEFs

Plat-E cells were seeded at 850k per 6-well onto 6-well plates coated g/ The next day, ~80% confluent Plat-E cells were transfected with 1.8 μg of DNA per well using a 4-5:1 ratio of μg PEI:μg DNA. The next day, a media change was performed with 1.25 mL fresh DMEM supplemented with 10% FBS and 25 mM HEPES to help buffer. MEFs were also seeded at 10k per 96-well onto 96-well plates coated with 0.1% gelatin. The next day, viral supernatant was collected, filtered through a 0.45 μm filter, and 1.25 mL fresh DMEM supplemented with 10% FBS and 25 mM HEPES was added again to the Plat-E cells. MEFs were transduced with 11 μL of viral supernatant per viral cassette. Fresh DMEM supplemented with 10% FBS was added to reach a final volume of 100 μL per 96-well. 5 μg/mL polybrene was supplemented to increase transduction efficiency. Transduction was repeated for a second day. One day after the second viral transduction was considered 1 dpi and 100 μL per 96-well fresh media was swapped in. At 3 dpi, media was switched to N3 media (DMEM/F-12 supplemented with N2, B27, and neurotrophic growth factors, BDNF, CNTF, GDNF, FGF all at 10 ng/mL).[23,52] For conditions with RepSox, 7.5 μM RepSox was also supplemented into the N3 media starting at 3 dpi. For experiments needing larger well sizes, MEF seeding and viral supernatant volumes were scaled accordingly by well surface area.

Quantification of conversion yield, purity, and efficiency

Converted cells were dissociated using 0.025% Trypsin-EDTA prior to 6 dpi and DNase/papain from 6 dpi onwards. One vial of papain (>100 U/vial) and one vial DNase (>1,000 U/vial) were dissolved in 6 mL of DMEM/F-12. 50 μL of this dissociation media was used per 96-well. Cells were incubated with dissociation media at 37°C, 5% CO_2 for ~15 minutes or until starting to detach. 100 μL of media was added to neutralize the reaction, then cells were resuspended in 300 μL PBS. All cells in a well were recorded using flow cytometry to detect Hb9::GFP fluorescence. iMNs were defined by gating the brightest Hb9::GFP fluorescent cells (Figure S1A).[23] Yield was calculated by dividing the total number of Hb9::GFP positive cells detected via flow by the total number of initially seeded cells which was generally 10k/96-well. Purity was calculated by dividing the total number of Hb9::GFP positive cells

Please cite this article in press as: Wang et al., Proliferation history and transcription factor levels drive direct conversion to motor neurons, Cell Systems (2025), https://doi.org/10.1016/j.cels.2025.101205

by the total number of cells detected via flow. Efficiency was calculated by dividing the total number of Hb9::GFP and mRuby2 positive cells by the total number of mRuby2 positive cells detected via flow.

$$\text{Yield}\ (\%) = \frac{\#\ \text{Hb9::GFP positive cells}}{\#\ \text{initial seeded cells} = 10\text{k}} \times 100\%$$

$$\text{Purity}\ (\%) = \frac{\#\ \text{Hb9::GFP positive cells}}{\#\ \text{total cells detected}} \times 100\%$$

$$\text{Efficiency}\ (\%) = \frac{\#\ \text{Hb9::GFP and mRuby2 positive cells}}{\#\ \text{mRuby2 positive cells}} \times 100$$

CellTrace labeling to measure cellular proliferation

At 1 dpi, cells were first washed with PBS. Then 100 μL/96-well of 1μM CellTrace-Far Red or 5μM CellTrace-Violet in PBS was added. Cells were incubated at 37°C, 5% CO_2 for 30 minutes. Then the staining solution was removed, cells were washed with media to remove residual stain, then fresh media was added. Cells were then cultured or converted as normal. CellTrace fluorescence was detected by flow cytometry. Cells that undergo a period of hyperproliferation were identified by dilution of CellTrace dye over 72 hours from 1 to 4 dpi for MEF conversion and over 144 hours from 1 to 7 dpi for human conversion. We denote cells with a history of rapid proliferation at the time point assayed as hyperproliferative (hyperP) and all other cells at 4 dpi as non-hyperP relative to the CellTrace dilution in a control puro infection condition to account for effects on proliferation induced by viral transduction. For MEF and human conversion, hyperP cells are defined relative to the 20%-lowest and 5%-lowest fluorescent cells, respectively, in a control puro infection condition for a given biological replicate.

Flow cytometry and FACS

An Attune NxT Acoustic Focusing Cytometer was used for flow cytometry analyzer experiments. A 405 nm laser with a 440/50 filter was used for blue fluorescence (DAPI, CellTrace-Violet), a 488 nm laser with 510/10 filter was used for green fluorescence (GFP), a 561 nm laser was used with 585/16 filter for red fluorescence (Alexa Fluor 594, mRuby2), and a 638 nm laser with a 670/14 filter was used for far red fluorescence (Alexa Fluor 647, CellTrace-Far Red, Zombie NIR). FSC-A and SSC-A were used to gate cells, while FSC-H and FSC-A were used to gate singlets using FlowJo. Singlets were exported as csv files to analyze using Python.

FACS was performed using a BD FACSAria. A 488 nm laser with 530/30 filter was used for green fluorescence (GFP), a 561 nm laser with 610/20 filter was used for red fluorescence (mRuby2) and a 640 nm laser with a 670/30 filter was used for far red fluorescence (CellTrace-Far Red). Cells were sorted into N3 media supplemented with penicillin-streptomycin. For replating experiments, cells were resuspended in their appropriate medias, counted, and replated at 10k/96-well. Penicillin and streptomycin were included for the rest of conversion after sorting.

For all cytometry experiments, appropriate controls were included to assess negative populations (*e.g.* un-stained cells, single color controls, secondary antibody only controls, non-targeting antibody controls, etc.).

Fixation and immunofluorescent staining

For plate imaging, cells were fixed with 3.7% paraformaldehyde for 1 hour at 4°C. Cells were washed three time with cold PBS and permeabilized with 0.5% Tween/PBS overnight at 4°C. Cells were then blocked with 5% FBS and 0.1% Tween/PBS for 1 hour at 4°C. Cells were then incubated with primary antibody diluted in blocking solution (5% FBS and 0.1% Tween/PBS) overnight at 4°C. Cells were then washed three times with cold 0.1% Tween/PBS, with the third wash being left for at least 20 minutes. Cells were then incubated with secondary antibody diluted in blocking solution (5% FBS and 0.1% Tween/PBS) for 1 hour at 4°C. Cells were then washed three times with cold 0.1% Tween/PBS and 0.1 μg/mL DAPI staining was added for 10 minutes. Cells were washed three more times with cold 0.1% Tween/PBS and imaged. In between incubation steps, the plate was kept covered in foil.

For flow cytometry, cells were dissociated and fixed with 3.7% paraformaldehyde for 15 minutes at room temperature. Cells were permeabilized by 200 μL of 0.5% Tween/PBS for 15 minutes at room temperature, and washed with PBS. 200 μL of primary antibody diluted in blocking solution (5% FBS and 0.1% Tween/PBS) was added and incubated at 4°C for 2 hours or overnight with rotation for mixing. Cells were washed three times with 1 mL cold 0.1% Tween/PBS, with the third wash being left for at least 30 minutes at 4°C. Cells were then incubated with 800 μL of secondary antibody diluted in blocking solution for 30 minutes at 4°C and washed three times with 1 mL cold 0.1% Tween/PBS. In between incubation steps, cells were kept covered in foil. The primary antibodies used in this study were: rabbit anti-Ki67 (1:100, GeneTex, GTX1667, RRID:AB_422351); mouse anti-TUBB3 (1:500, Biolegend, 801202, RRID:AB_10063408); rabbit anti-MAP2 (1:500, Cell Signaling Technology, #4542, RRID:AB_10693782). The secondary antibodies used in this study were: donkey anti-mouse Alexa Fluor 647 (1:500, Invitrogen, A-31571, RRID: AB_162542); donkey anti-rabbit Alexa Fluor 594 (1:500, Invitrogen, A-21207, RRID: AB_141637); donkey anti-rabbit Alexa Fluor 647 (1:500, Invitrogen, A-31573,

Please cite this article in press as: Wang et al., Proliferation history and transcription factor levels drive direct conversion to motor neurons, Cell Systems (2025), https://doi.org/10.1016/j.cels.2025.101205

RRID:AB_2536183); goat anti-mouse Alexa Fluor 488 (1:500, Jackson ImmunoResearch Labs, 115-546-146, RRID: AB_2338868).

Morphology quantification of Hb9::GFP-positive cells

Cells were fixed as described above and stained with DAPI as a nuclear marker. Random images were taken such that at least >100 Hb9::GFP-positive cells were imaged per condition per biological replicate. Hb9::GFP-positive cells with neuronal morphology were classified as having a tight soma with neurites. Annotation was performed manually using ImageJ.

5-ethynyl-2'-deoxyuridine (EdU) assay to detect cell cycle progression

Cells were sorted by FACS for Hb9::GFP at 14 dpi and replated at a density of 120k cells per 24-well coated with 0.1% gelatin for at least 10 minutes at room temperature. Control DDRR cells were sorted by singlets with no fluorescent gating. Cells were recovered in N3 media with RepSox and penicillin-streptomycin. Half-media changes were performed every other day to prevent cell loss. For aphidicolin-treated control cells, 1 μM aphidicolin was added 24 hours before EdU, from 6 to 7 days post-sort (dps), to block DNA replication prior to EdU-addition. Then 10 μM EdU was fed to all cells for 24 hours at 7 days post-sort (dps) until 8 dps. Thus, aphidicolin control cells were treated with aphidicolin for a total of 48 hours from 6 to 8 dps. Cells were then dissociated with DNase/papain as described above and clicked according the manufacturer's recommendation using the Click-iT EdU Alexa Fluor 647 Flow Cytometry Assay Kit.

Brn2-2A-mRuby2 multiplicity of infection (MOI) calculation and conversion assay

Plat-E cells were seeded at 850k per 6-well onto 6-well plates coated with 0.1% gelatin for at least 10 minutes at room temperature. The next day, ~80% confluent Plat-E cells were transfected with 1.8 μg of DNA per well using a 4-5:1 ratio of μg PEI:μg DNA. The next day, a media change was performed with 1.25 mL fresh DMEM supplemented with 10% FBS and 25 mM HEPES to help buffer. The next day, viral supernatant was collected, filtered through a 0.45 μm filter, and 1.25 mL fresh DMEM supplemented with 10% FBS and 25 mM HEPES was added again to the Plat-E cells. The next day, viral supernatant was collected and filtered through a 0.45 μm filter again for approximately ~2.2 mL of viral supernatant. 1 volume Lenti-X concentrator was added to 3 volumes viral supernatant and incubated at 4°C overnight. The virus was pelleted by centrifugation at 1,500 x g for 45 minutes at 4°C. The supernatant was removed, and the pellets were resuspended in DMEM with 10% FBS to a final volume of 200 μL per original 2.2 mL of viral supernatant. Several wells would be mixed together, aliquoted, and frozen at -80°C as a single batch.

To determine MOI, MEFs were transduced with 1:2 serial dilutions of frozen virus. Frozen viral supernatant was resuspended in DMEM swith 10% FBS to reach a final volume of 100 μL per 96-well. 5 μg/mL polybrene was supplemented to increase transduction efficiency. A single transduction was performed and mRuby2 expression was measured at 4 dpi. The percent of mRuby2-positive MEFs at 4 dpi vs. virus volume was plotted and fit to a Poisson distribution to determine the number of transducing units (TU) per volume per 10k seeded MEFs for a given frozen batch. Typical volumes we observed to reach an MOI of 5 TU/cell were around ~2 μL/96-well for 10k seeded MEFs/96-well in 100 μL total transduction media with polybrene using this method.

For comparing mRuby2 vs. bulk populations, either an FSC-A vs. mRuby2-A gate was used for mRuby2-positive cells or FSC-A vs. FSC-H for bulk cells. For hyperproliferation by CellTrace-Violet dilution, the dimmest 20% in Ctrl-puro bulk population was used to set the CellTrace-Violet gate. Two twin plates were converted per biological replicate. The yield normalized to 4 dpi count was calculated as follows for a given biological twin:

$$\text{Yield normalized to 4 dpi counts (\%) for bulk} = \frac{\#\,\text{Hb9::GFP+at 14 dpi}}{\#\,\text{singlets at 4 dpi}} \times 100$$

$$\text{Yield normalized to 4 dpi counts (\%) for } \textbf{mRuby2} + = \frac{\#\,\text{Hb9::GFP+AND}\ \#\,\text{mRuby2+at 14 dpi}}{\#\,\text{mRuby2+at 4 dpi}} \times 100$$

Twin conversion assays for 4 dpi exogenous transgene reporter and 14 dpi conversion

MEFs from a single biological source were seeded in duplicate and converted using six uORF conditions (five uORFs and one without any uORFs) with the same viral supernatant mixes, such that each twin received the same exact transduction treatments. At 1 dpi, one biological twin was stained with CellTrace-Violet to assay at 4 dpi for proliferation history and exogenous transgene expression via the mRuby2 reporter. The other biological twin was kept until 14 dpi to measure conversion yield and purity. Each twin was performed with three technical replicates and the results were averaged and plotted against each other for each biological replicate. Thus, each point represents the average geometric mean of mRuby2 expression at 4 dpi across three wells and the average conversion rate at 14 dpi across another three wells, for a total of six wells assayed for a single biological replicate of one condition.

Ngn2-2A-mRuby2 and proliferation history dual sort

Cells were transduced and stained with CellTrace-Violet as described above. At 4 dpi, cells were sorted by both their proliferation history and mRuby2 levels using FACS, as described above. An additional unused far red CellTrace-Far Red-A vs. mRuby2-A

Please cite this article in press as: Wang et al., Proliferation history and transcription factor levels drive direct conversion to motor neurons, Cell Systems (2025), https://doi.org/10.1016/j.cels.2025.101205

gate was used to gate mRuby2-positive cells. It was found that gating on Far Red vs. Red resulted in better separation on the BD FACSAria than FSC vs. Red. Ngn2-2A-mRuby2 levels were then gated into quartiles (0-25%, etc…) based on the mRuby2-positive cells. Cells were sorted and replated at 10k/96-well onto 0.1% gelatin-coated plates and converted until 14 dpi.

Viral transduction and iMN conversion of human adult dermal fibroblasts

HEK293Ts were seeded at 6.5 million per 10 cm dish onto 10 cm dishes coated with 0.1% gelatin. The next day, each dish of 293Ts was transfected with 10.8 ug pLK-packaging plasmid, 1.2 ug of pHDMG envelope plasmid, and 12 ug of transfer plasmid using a 4-5:1 ratio of ug PEI:μg DNA. 6–8 hours later, a media change was performed with 6.5 mL of 25 mM HEPES buffered DMEM with 10% FBS. 24, 48, and 72 hours later, viral supernatant was collected and stored at 4°C and was replaced with fresh media after the first two collections. After the third collection, the viral supernatant was filtered with a 0.45 μM filter and was mixed with 1 volume Lenti-X concentrator to 3 volumes viral supernatant and incubated at 4°C for 1-3 days. Next, the virus was pelleted by centrifugation at 1,500 x g for 45 minutes at 4°C. The supernatant was removed, and the pellets were resuspended in HDF media to a final volume of 200 μL per 10 cm dish. The virus was stored for less than a week at 4°C until use. HDFs were seeded one day prior to transduction onto plates coated with 0.1% gelatin at the appropriate seeding density (e.g. 2.5k, 5k, or 10k per 96-well). HDFs were transduced two days in a row with 5 μL of each concentrated virus per 96-well. Fresh HDF media was included to reach a final volume of 100 μL per 96-well, and 5 ug/mL polybrene was added to increase transduction efficiency. Each day after the addition of virus, the plates were centrifuged at 1500 x g for 90 minutes at 32°C to further increase transduction efficiency via spinfection. At 1 dpi and 4-5 dpi, the media was replaced with fresh HDF media. At 7 dpi, the cells were dissociated using trypsin. Once the cells were in suspension, fresh HDF media was added, and the contents of each well were transferred to a laminin coated plate. The day after replating, the media was replaced with N3 media with RepSox. N3 media was replaced every 3 to 4 days until 35 dpi.

Morphology quantification of human iMNs

Neuronal clustering in the high-efficiency LNI DD ABC condition made traditional Sholl analysis challenging. Instead, all images of human iMNs were analyzed from the experiments shown in Figure 7. We quantified the number of neuron clusters observed in each field of view across the different conditions. For each iMN cluster, the number of axons or axonal bundles projecting from each cluster was manually counted as an indicator of the number of iMNs in each cluster.

Fluorescent imaging

Images not taken for immunohistochemistry were imaged using a Keyence All-in-one fluorescence microscope BZ-X800.

QUANTIFICATION AND STATISTICAL ANALYSIS

Quantification and statistical analysis were performed using Python.